Journal of Nanobiotechnology

RESEARCH

Open Access

Structurally and functionally optimized silk fibroin-alginate-based biomimetic scaffolds reinforced with nanobioceramics for bone tissue engineering applications

Thanh-Mai Ngoc Nguyen[2,1†], Ngoc-Han Hoai Le[2†], Mohanapriya Murugesan[3†], Gopinathan Janarthanan[4], Panchanathan Manivasagan[5], Cuong Hung Luu[6], Diep Phan[9], Eue-Soon Jang[5], Yi Li[7], V. H. Giang Phan[2], Sanjairaj Vijayavenkataraman[4*], João Conde[8*] and Thavasyappan Thambi[3,10*†]

Abstract

In this study, we prepared chemically crosslinked silk fibroin (SF) and sodium alginate (Alg) biomimetic scaffolds reinforced with bioceramic nanohydroxyapatite (nHAp) for bone tissue engineering (BTE) applications. The pore sizes of these scaffolds were effectively controlled by varying the composition of the SF/nHAp/Alg biocomposites. The scaffold prepared with a 40:20:40 SF: nHAp: Alg ratio exhibited excellent swelling properties, reaching over 1700% within 70 min. In vitro degradation studies demonstrated that these biomimetic scaffolds exhibited controlled degradation, taking over 30 days to achieve 50% degradation. The scaffolds also showed good mechanical properties; they maintained structural integrity and did not break, even under a load approximately 800 times their own weight. Additionally, scaffolds loaded with synthetic peptide salmon calcitonin effectively controlled initial burst release and enabled sustained therapeutics delivery for up to two weeks. The biocompatibility of the scaffolds was evaluated using *in vitro* cell viability and hemolysis assays, which revealed good safety for human dermal fibroblast cells and negligible toxicity to rabbit red blood cells. Importantly, the scaffolds promoted cell proliferation and alkaline phosphatase secretion in human bone marrow stem cells. Histological and immunological analyses in a scaffold-implanted mouse model have demonstrated biocompatibility, supporting osteoclastic resorption and osteoblastic mineralization by downregulating RANKL. Furthermore, the chick chorioallantoic membrane assay showed the excellent angiogenic properties of the scaffold.

†Thanh-Mai Ngoc Nguyen, Ngoc-Han Hoai Le, Mohanapriya Murugesan contributed equally to this work.

*Correspondence:
Sanjairaj Vijayavenkataraman
vs89@nyu.edu
João Conde
joao.conde@nms.unl.pt
Thavasyappan Thambi
thambi@khu.ac.kr

Full list of author information is available at the end of the article

These results suggest that the bioceramic-reinforced SF/Alg biomimetic scaffold has significant potential for use in BTE.

Keywords Silk fibroin, Hydroxyapatite, Alginate, Salmon calcitonin, Scaffold, Bone tissue engineering

Introduction

Injuries, aging, congenital disorders, and diseases can lead to damage and malfunction of bone tissues in the human body, affecting more than 15 million people worldwide [1–3]. The growing demand for orthopedic surgical procedures has significantly increased the need for bone substitutes for transplantation [4, 5]. Owing to the inherent regenerative ability of human bone, small defects are frequently treated using the patient's native bone tissue, a method known as autologous bone transplantation [6]. For larger, critical-sized, or non-healing bone defects, orthopedic surgeons commonly use allografts, which involve bone taken from a donor [7, 8]. However, these healing processes are lengthy and post-recovery bone incompatibility can cause various complications. Tissue regeneration involves regenerating damaged tissues by assembling appropriate functional constructs at the defect site, which can restore or remodel damaged tissues or organs [9, 10]. The integral elements required for bone tissue engineering (BTE) include a porous three-dimensional scaffold to serve as a natural site for tissue growth, osteogenic cells to form new tissue, signaling molecules released after defects for repair, and a bioreactor to provide the necessary culturing conditions to induce bone growth [11–13]. Scaffolds, a significant component of BTE, serve as temporary matrices for cells to restore their function and regenerate tissues [14]. They provide a suitable space and microenvironment to support cell adhesion, migration, proliferation, and delivery of biochemical factors [15]. Hence, choosing appropriate materials is a crucial step in scaffold construction, as their properties—such as osteoinductive and osteoconductive capabilities, angiogenic properties, biocompatibility, and brittleness—play a significant role in determining the scaffold's effectiveness.

The mulberry silkworm (Bombyx mori) is a major insect cultivated for silk production [16]. Silk fibroin (SF), the primary structural protein of silk, is a natural biopolymer composed of fibroin chains and associated glycoproteins, which together confer its remarkable mechanical strength and biocompatibility [17, 18]. The light chain possesses high hydrophilicity and elasticity, and its function is responsible for maintaining the structural integrity [19]. The heavy chain's hydrophobic domain contains a repeating amino acids sequences (Gly-Ser-Gly-Ala-Gly-Ala), along with charged amino acids such as lysine, arginine, glutamic acid, and aspartic acid [20]. These hydrophobic blocks can form antiparallel β-sheets through hydrogen bonding and hydrophobic interactions [21]. This natural polymer exhibits a range of outstanding properties including easy modification, thermal stability, degradability, and excellent mechanical strength [19, 22]. Moreover, functional SF has potential applications in drug delivery. However, scaffolds made of SF alone are poorly soluble under physiological conditions. Hydroxyapatite (HAp), chemically represented as $Ca_{10}(PO_4)_6(OH)_2$, is a mineral component of human bone, making up 50–70% of its inorganic constituents, and closely resembles the extracellular matrix of bone [23, 24]. HAp can integrate with native bone tissue and promote induction of new bone, thereby supporting the regeneration and repair of damaged bone [25]. Moreover, HAp has been shown to regulate local Ca^{2+} concentrations, effectively inducing osteoblast proliferation and promoting mesenchymal stem cell differentiation [26, 27]. The controlled and localized release of bioactive ions from HAp contributes significantly in angiogenic modulation and cellular activity, facilitating bone healing through stimulation of cell proliferation, differentiation, and vascularization [28, 29].

Sodium alginate (Alg), a naturally occurring polymer extracted from algae, has been extensively used for biomedical applications [30–32]. Alg is composed of repeating units of β-D-mannuronic acid and α-L-guluronic acid residues, which can undergo ionic crosslinking with cations such as Ca^{2+} [33]. Alg has been widely investigated owing to its ease of chemical modification, biocompatibility, biodegradability, and low toxicity [34]. Owing to the presence of multiple functional groups, Alg allows for dual crosslinking, where secondary ionic crosslinking occurs after the initial chemical crosslinking. However, with Ca^{2+}-based secondary crosslinking, calcium ion leaching from the gel network may weaken its structure under physiological conditions. Therefore, chemical crosslinking is essential to ensure the stability of the scaffolds [35]. The incorporation of natural SF and bioceramic HAp into Alg-based scaffolds improves their mechanical properties and supports cell adhesion, growth and bone regeneration [36]. For instance, biomimetic Alg/SF scaffolds were successfully fabricated by Meng et al. using supercritical CO_2 technology, demonstrating excellent biocompatibility with no obvious cytotoxicity, enhanced cell adhesion, and superior support for L929 fibroblast proliferation compared to pure SF scaffolds [37]. Spessot et al. developed biomimetic SF sponges bone tissue engineering, with the inclusion of HAp enhancing structural stability, bioactivity, and osteosarcoma cell metabolism [38]. Dual-crosslinked

Alg/Oxidized Alg/SF hydrogels, formed via ionic gelation and Schiff-base reactions, exhibited enhanced mechanical strength, improved biocompatibility, and promoted bone marrow mesenchymal stem cell differentiation [39]. A multistage porous HAp/SF composite scaffold, fabricated using electric field-induced gel technology, exhibited a biomimetic hierarchical structure, enhanced mechanical properties comparable to cancellous bone, and optimal cell responses, effectively balancing porosity, mechanical strength, and degradation for bone tissue regeneration [40]. While these studies provide promising insights into scaffold design for bone regeneration, they are constrained by the inherent trade-off between achieving a biofriendly porous structure, suppressing proinflammatory cytokines, activating osteoblast differentiation genes, maintaining controlled degradation rates, and ensuring in vivo safety.

To address these challenges and optimize scaffold performance, careful selection of matrix components and crosslinking agents plays a crucial role in enhancing mechanical stability, bioactivity, and controlled release properties for bone tissue engineering applications. Structural and functional optimization of scaffolds is crucial for enhancing their mechanical stability, bioactivity, and controlled release properties. In this study, scaffold properties were tuned through careful selection of matrix components, including SF, bioceramic nanohydroxyapatite (nHAp), and Alg, each contributing unique advantages. SF enhances mechanical strength and biocompatibility, nHAp improves osteoconductivity, and Alg aids in controlled drug release. Furthermore, different crosslinking agents such as glutaraldehyde (GA) and 1,4-butanediol diglycidyl ether (BDDE) were investigated to modify the physicochemical properties of the scaffolds, ensuring stability while maintaining biocompatibility. The rationale behind exploring various crosslinkers stems from their ability to influence degradation rate, mechanical integrity, and cellular interactions, ultimately optimizing the scaffold for bone tissue engineering applications. The balance between these matrix components and crosslinkers was systematically evaluated to achieve an optimal formulation, where mechanical properties, drug release kinetics, and bioactivity were considered in a synergistic manner. Therefore, the objectives of this study were to (i) develop silk fibroin–based scaffolds incorporating nHAp, alginate, and calcitonin for bone tissue engineering; (ii) investigate the influence of different crosslinkers (GA and BDDE) on the mechanical, physical, and biological properties; (iii) characterize the structural, mechanical, and degradation properties of the scaffolds; and (iv) evaluate the in vitro calcitonin release profile and the in ovo biocompatibility and angiogenic potential using the CAM assay.

Furthermore, we evaluated the biomimetic scaffold's ability to release salmon calcitonin (SC) in a controlled, sustained manner to support tissue regeneration (Figure 1). SC is a calcitropic polypeptide widely used in clinical practice, particularly for the treatment of brittle bone diseases [41]. As a regulatory hormone, SC modulates calcium homeostasis by interacting with osteoblasts, recruiting stem cells, and inhibiting osteoclastic bone resorption through binding to specific surface receptors [42–44]. Moreover, SC has been shown to enhance bone mineralization and regulate bone formation [42], making it a promising therapeutic agent for promoting bone regeneration. Incorporating SC into biomaterial scaffolds allows for localized, sustained delivery at the defect site, which could improve its efficacy in bone tissue engineering applications. Bradford assay was used to determine the release of SC from the scaffolds. The biocompatibility and hemocompatibility of the scaffolds were tested using human dermal fibroblast (HDF), human mesenchymal stem cells, and rabbit red blood cells. An *in ovo* assay was performed on chick embryos to evaluate the biocompatible and angiogenic properties of the scaffolds. In addition, the in vivo safety of the biomimetic scaffolds was examined by subcutaneously implanting them into BALB/c mice. Gene expression analysis was conducted to confirm the transcriptional changes following the implantation of the biomimetic scaffolds.

Materials and methods

Materials

Calcium chloride ($CaCl_2$, ≥ 98%), sodium carbonate (Na_2CO_3, ≥ 99.5%), phosphate buffered saline (PBS, pH 7.4), and dialysis tubing cellulose membrane (MWCO: 3,500 Da) were obtained from Sigma-Aldrich (MO, USA). GA and BDDE were purchased from Shanghai Macklin Biochemical Co., Ltd (China). Ethyl alcohol (C_2H_5OH, ≥ 99.5%), ammonia solution (NH_4OH), diammonium hydrogen phosphate ($(NH_4)_2HPO_4$, ≥ 99.0%), calcium nitrate tetrahydrate ($Ca(NO_3)_2.4H_2O$, ≥ 99.0%), and phosphoric acid (H_3PO_4) were provided by Guangdong Guanghua Sci-Tech Co., Ltd. (China). Sodium Alginate (Alg) was provided by Duchefa Biochemie B.V. (Haarlem, Netherlands). Coomassie Brilliant Blue G-250 (CBB) was obtained from HiMedia Laboratories Pvt., Ltd. (India). Calcitonin salmon (SC) 50 IU/ml was supplied by Lisapharma (Italy). The mulberry silkworm (*Bombyx mori*) originated from Lam Dong, Da Lat, Vietnam.

Preparation of SF solution

SF solution was prepared by slightly modifying a previously reported procedure [22]. Initially, cocoons were cut into small pieces and degummed in a 0.02 mol/L boiling Na_2CO_3 solution at 80–90 °C for 40 min to remove sericin and impurities. Subsequently, the silk was thoroughly

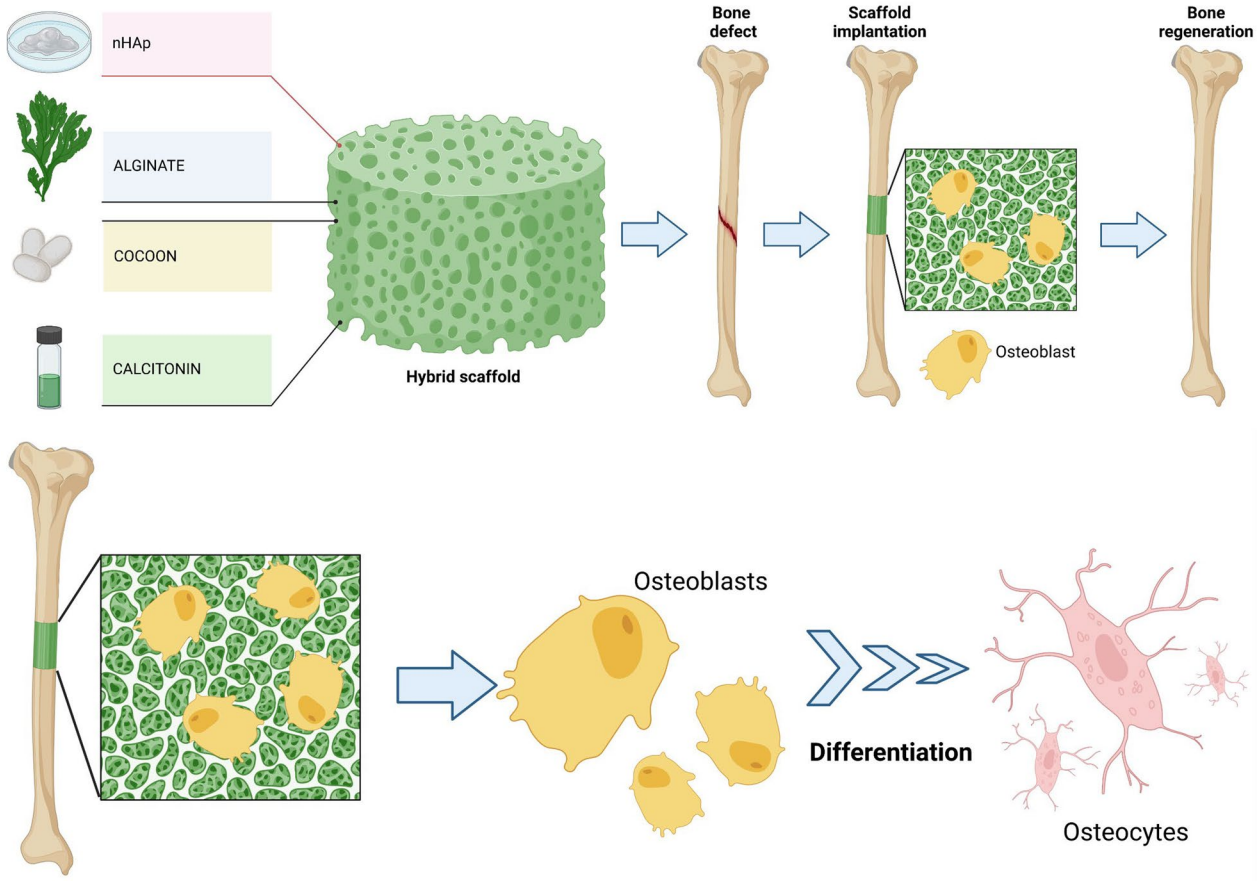

Fig. 1 Schematic illustration of the preparation of a biomimetic scaffold. The biomimetic scaffold was constructed using nHAp, Alg, and SF, with salmon calcitonin incorporated into the scaffold through a simple soakingmixing process. model to evaluate inflammatory, osteogenic, and safety responsesThis scaffold exhibits great potential for bone tissue regeneration

washed with distilled water for 5 min at 50 °C. This procedure was repeated three times. The silk fiber (3 g) was dehydrated in an oven at 60 °C for 3 h and subsequently dissolved in a mixture of $CaCl_2$ (7.7 g), EtOH (8.1 mL), and H_2O (10 mL) at a molar ratio of 1:2:8, at 75–85 °C for 30 min. The resulting solution was placed in a dialysis membrane (MWCO: 3,500 Da) and dialyzed using DW for 3 days. The aqueous silk solution was then centrifuged at 6000 rpm for 10 min at 4 °C to remove remaining impurities, and the supernatant was collected and stored at 4 °C.

Synthesis of nHAp

nHAp was synthesized via wet chemical precipitation [45] using $Ca(NO_3)_2.4H_2O$ and $(NH_4)_2HPO_4$. Initially, a suspension of $Ca(NO_3)_2.4H_2O$ (0.15 mol/L) and $(NH_4)_2HPO_4$ (0.09 mol/L) was vigorously stirred to maintain a Ca/P molar ratio of 1.67. NH_4OH solution was then added to adjust the pH of the reaction mixture to 10–12. The mixture was constantly stirred at 90 °C for 2 h. The resulting white precipitate was washed four to five times with distilled water, filtered, and dried at 100 °C for 2 h. After crushing into powder form, the material was calcined at 900 °C for 5 h to yield nHAp. The chemical reaction involved in the preparation of nHAp can be summarized as follows:

$$10Ca(NO_3)_2.4H_2O + 6(NH_4)_2HPO_4 + 8NH_4OH \rightarrow Ca_{10}(PO_4)_6(OH)_2 + 20NH_4NO_3 + 46H_2O$$

Fabrication of scaffold

To fabricate scaffolds, separate solutions of Alg, SF, and nHAp were prepared in individual flasks. Initially, a 1.5% (w/v) Alg solution was prepared by dissolving alginate in water and stirring vigorously at 60 °C for 1 h. Simultaneously, a 6% (w/v) SF solution was prepared in distilled water. In parallel, a 0.5% (w/v) solution of nHAp was homogeneously dispersed in distilled water using an ultrasonic homogenizer. As outlined in Table 1, the three components were mixed at various volume ratios and stirred for 30 min. Subsequently, a solution of GA (0.5%, w/v) or BDDE (60%, w/v) was introduced into the mixture and continuously stirred for further 60 min at 45 °C to crosslink the SF and Alg components. The resulting mixture was poured into molds and allowed to gelation

Table 1 Composition of scaffolds

	SF(6 wt.%)	nHAp (0.5 wt.%)	Alg (1.5 wt.%)	PBS (pH 7.4)	Cross-linker
SF/nHAp	0.4 mL	0.2 mL	-	0.5 mL	-
SNAX	0.4 mL	0.2 mL	0.4 mL	0.1 mL	-
SNAG	0.4 mL	0.2 mL	0.4 mL	-	0.1 mL of GA 0.5 wt.%
SNAB	0.4 mL	0.2 mL:	0.4 mL	-	0.1 mL of BDDE 60 wt.%

at room temperature for a day. The frozen hydrogels were then freeze-dried for three days to yield SF/HAp/Alg scaffolds crosslinked with GA or BDDE (referred to as SNAG or SNAB). Additionally, scaffolds without cross-linkers were prepared, termed SNAX, and used as controls.

Methods

^{1} H NMR spectra

The chemical structures of SF and scaffolds were characterized using ^{1}H NMR spectra (Varian Unity Inova 500 SNB). The NMR analysis was performed in accordance with ASTM E3866-21: Standard Guide for Nuclear Magnetic Resonance Spectroscopy of Polymers to ensure data reliability.

X-ray diffraction (XRD) analysis

A Bruker X-ray Diffractometer was used to analyze the crystallographic structure of the nHAp. The XRD analysis was conducted following ASTM D2624-15: Standard Test Method for X-Ray Diffraction of Polymers, ensuring standardized data acquisition and interpretation.

Fourier-transform infrared (FT-IR) spectra

FT-IR spectroscopy (PerkinElmer, USA) was used to characterize the cross-linked scaffold, the β-sheet conformation, and other functional groups.

SEM imaging

The cross-sectional morphology, structure, and pore size of SF, SF/nHAp, SNAX, SNAG and SNAB were observed using SEM (JSM-IT100, Japan).

UV-Vis spectra

Bradford reagent was applied to determine the spectrophotometric absorbance of SC using a UV-Vis spectrophotometer (Shimadzu UV-1800, Japan) at a wavelength of 595 nm.

Porosity

Initially, the scaffolds were cut into cylinder shapes (12 mm in diameter × 10 mm in height), and their weights were recorded in the dried state (W_0), along with their dimension, to compute their volume (V). Subsequently, the samples were submerged in absolute ethanol at room temperature for 30 min. Afterward, they were withdrawn from the solvent, any remaining ethanol was removed, and their weights were measured again (W_1). This experiment was performed in triplicate for each scaffold type with varying formulations.

The porosity of the scaffold was determined using the following equation [46], whereas ρ is density of the ethanol:

$$\boldsymbol{Porosity}\,(\%) = \frac{W_1 - W_0}{\rho V} \times 100\%$$

Mechanical strength

Scaffolds must maintain structural stability after implantation into anatomical sites to ensure robust load-bearing reconstruction [47, 48]. It is imperative that they maintain sufficient mechanical strength until the regenerated bone tissue can take over its structural function. In this study, the compressive strength was assessed on a texture analyser (TA.XTplus, Stable Micro Systems, United Kingdom). The cylindrical shape samples with diameter of 12 mm and height of 10 mm were compressed to 70% strain at speed of 10% strain/min. The compressive strength is determined at 30% compressive strain. The compressive mechanical testing was conducted in accordance with ASTM F2150-19: Standard Guide for Characterization and Testing of Biomaterial Scaffolds Used in Tissue-Engineered Medical Products, which provide guidance for evaluating the compressive properties of porous biomaterial scaffolds.

Additionally, the stability under compressive load was simply evaluated by applying calibrated weights ranging from 1.0 g to 100 g on scaffolds and any changes in the shape of the scaffold was recorded to ascertain its stability.

Swelling ratio

To investigate swelling ability, the changing in weight of scaffolds before and after immersing in PBS was calculated [49]. Initially, the weight of scaffold samples (12 mm in diameter × 10 mm in height) was recorded in its dried state (W_0) and then soaked in PBS at pH 7.4 and 37 °C. At 10 min intervals, the samples were withdrawn, gently wiped to remove excess water, and weighed (W_t). This procedure was repeated three times for each sample to ensure data reliability of the experiment.

The swelling ratio was determined using the following equation [32]:

$$\boldsymbol{Swelling\ ratio}\,(\%) = \frac{W_t - W_0}{W_0} \times 100\%$$

In vitro stability and degradability

The stability of the scaffolds was assessed in a PBS (pH 7.4) environment over a period of 30 days with the aim of establishing a reference for the duration required for complete bone regeneration. The scaffolds (12 mm in diameter × 10 mm in height) were submerged in this solution and closely monitored, and the results were meticulously recorded to ascertain their stability within a living human body.

Degradability is vital attribute of a scaffolds for tissue engineering application, as it relies on providing temporary templates that assemble into the native ECM to promote tissue repair and regeneration. This process is closely linked to biocompatibility, as the degradation products must be nontoxic and capable of being metabolized and eliminated from the body. This degradation behavior can be observed through the mass reduction of the scaffold over a period of several weeks in vitro. For the degradation test, scaffolds were incubated in PBS solution (pH 7.4) at 37 °C. The initial weight (W_0) and the weight of degraded scaffold (W_t) after removal from incubation medium and lyophilization were documented at specific time points each 5 days, and the experiment was repeated three times for each sample. The experiment lasted for 30 days and the degradation degree was calculated using following equation [50]:

$$\boldsymbol{Degradation}\,(\%) = \frac{W_0 - W_t}{W_0} \times 100\%$$

In vitro release of SC

In the Bradford method, Coomassie Brilliant Blue G-250 (CBB) was used to quantify the protein concentration in release environment. The SC polypeptides were evaluated by their binding to the Bradford dye under acidic condition, resulting in a colorimetric shift from brown to blue, and the change in absorption was measured at λ=595 nm. A standard curve was established using SC solutions of various concentrations (in the range of 2.0 - 20.0 μg/ml). SC was loaded into the scaffolds by the soaking method. The loading efficiency of SC in the scaffolds was first determined to quantify the amount of SC successfully incorporated into the scaffolds.

For in vitro drug release studies, the samples containing SC were immersed in PBS solution (pH=7.4). At specific time intervals, 0.5 mL of the medium was withdrawn and combined with 1.0 mL Bradford solution. Simultaneously, 0.5 mL of PBS solution was added to the soaking solution to compensate for the lost volume, and this process was continued until the completion of the release test. The release of SC from the scaffolds was measured over a period of 15 days, with samples collected at 1 day intervals.

Drug release behavior was determined according to the equation below [51]:

$$\boldsymbol{Cumulative\,release}(\%) = \frac{V_0 \times C_t + V \times \sum_{n=1}^{t-1} C}{W} \times 100\%$$

V_o denotes the total volume of the release medium, while V is the volume taken out at each specific time point, C_t represents the concentration of SC in the release medium at time t, C refers to the concentration of SC at the previous time point (t-1), and W indicates SC weight in the scaffold samples.

In vitro hemolysis assay

The hemocompatibility of the scaffolds was assessed using citrated blood samples. Red blood cells (RBCs) were isolated by centrifuging anticoagulated blood samples collected from rabbits at 3000 rpm for 20 min, followed by two washes with PBS. Subsequently, 0.2 mL of RBCs were mixed with 1.8 mL PBS, and scaffold sample was added to obtain the suspension. The suspension was incubated for 3 h at 37 °C, followed by centrifugation at 3000 rpm for 10 min. In this study, Triton X-100 and PBS were used as the positive and negative controls, respectively, and the absorbance value of the supernatant was measured at 540 nm.

The degree of hemolysis was computed using the equation below [52]:

$$\boldsymbol{Hemolysis}\,(\%) = \frac{OD_{sample} - OD_{negative\,control}}{OD_{positive\,control} - OD_{negative\,control}} \times 100\%$$

In ovo biocompatibility evaluation

To assess the biocompatibility of the prepared scaffolds, a chorioallantoic membrane of chicken embryo (CAM) assay was employed [53, 54]. On embryonic day 10, the eggshell was carefully opened by creating a small window under aseptic conditions in a laminar flow cabinet. The scaffolds (approximately 4 × 4 × 2 mm), sterilized by UV irradiation, were gently placed onto the CAM. To maintain local humidity and prevent desiccation, 30 μL of PBS was applied to each scaffold. The window was sealed with sterile parafilm, and the eggs were returned to the incubator. The eggs were retrieved at specified time points (12, 13 and 14) for examination of scaffold integration, angiogenic response, and embryo viability. For this study, 3 eggs/scaffolds were tested per group.

In vitro biocompatibility test and Live/Dead cell imaging

Human dermal fibroblasts (HDFs) were cultured in Dulbecco's Modified Eagle's medium (DMEM) supplemented

with 10% fetal bovine serum (FBS), 1% penicillin, and 1% streptomycin in a humidified atmosphere with 5% CO_2 at 37 °C. Human mesenchymal stem cells (hMSCs) were cultured according to standard protocols. hMSCs were cultured in DMEM supplemented with 10% FBS, 1 ng/mL basic fibroblast growth factor (bFGF), 1% non-essential amino acids (NEAA), 1% penicillin, and 1% streptomycin in a humidified atmosphere. Different scaffolds measuring 8 × 8 × 4 mm^3, were used in this study. The scaffolds were decontaminated with 70% ethanol for 30 min, rinsed three times with PBS, dried, and irradiated with UV light for 2h. Cells (2×10^4 cells in 100 μL) were seeded onto the scaffolds and placed in the center of the 24-well plates. After a 30 min incubation, 2 mL of culture medium was added to each well, and the cell-seeded scaffolds were cultured for the designated periods.

At different time points (1, 2, 3, and 5 days), the cell-seeded scaffolds were washed with PBS and treated with 100 μg/mL MTT [3-(4,5-dimethylthiazol-2-yl)–2,5-diphenyltetrazolium bromide] for 4 h at 37 °C. Subsequently, the scaffolds were washed with PBS and dissolved in 2 mL DMSO. The solubilized purple formazan in DMSO was quantified by measuring absorbance at 540 nm using an ELISA reader (Bio-TEK MQX200). Cells cultured in serum-free media alone served as negative controls.

Cell viability of the hydrogel scaffolds was investigated using a live/dead assay. HDF and hMSCs were cultured as described previously. Following the manufacturer's protocol, the cells were stained using a live/dead assay kit (Invitrogen R37601). Images were captured using an Olympus fluorescent microscope (Olympus, FV300).

In vitro scratch healing assay

A scratch-healing assay was used to study the migration of HDF. The cells were seeded in 12-well plates at a density of 50×10^3 cells/well. The culture medium was changed after 24 h of incubation. When the cells reached 70% confluency, a scratch was made using a 100 μL pipette tip. The cells were washed with PBS to remove the damaged cells. Thereafter, the hydrogel scaffold was placed in the wells and incubated. The cells were stained as described in the previous section, and time-dependent CLSM images were obtained using an Olympus (X53) microscope.

In vivo subcutaneous scaffold implantation

For the in vivo implantation of scaffolds, BALB/c mice (20–30 g, 6–8 weeks old) were purchased from the Korea Research Institute of Bioscience and Biotechnology (Daejeon, Korea). All the animal experiments were approved by the Institutional Committees of Kyung Hee University (Approval number: KHU-22–216). The animal experiments were complied with the National Research Council's Guide for the Care and Use of Laboratory Animals.

Before implantation, all animals were housed for two weeks in a controlled environment with unrestricted access to food and water. The mice were anesthetized using isoflurane prior to scaffold placement. The scaffolds were first decontaminated with 70% ethanol for 30 min, rinsed three times with PBS, dried, and sterilized under UV light for 2 h. Subsequently, pre-wetted scaffolds (8 mm in diameter × 2 mm in height) were implanted subcutaneously, and the incision sites were carefully sutured. Two weeks later, the mice were sacrificed, and blood samples and organs were collected for further analysis.

Histological analysis

For histological analysis, the major organs were fixed in 10% formalin for 48 h. The formalin-fixed tissues were dehydrated in graded ethanol and xylene, embedded in paraffin, and sectioned into 5–7 μm thick slices. The tissue sections were stained with hematoxylin and eosin (H&E) and examined under a light microscope (Carl Zeiss, Jena, Germany).

Cytokine analysis

Blood samples were obtained from the mice at two weeks post-implantation of the scaffold. For RT-PCR analysis, an equal amount of RNA was reverse-transcribed into cDNA and RT-PCR was performed to evaluate the expression of various proteins. Primers used in this study are listed in Table S1, Supporting Information. At the end of RT-PCR, the products were electrophoresed on a 1% agarose gel, and the bands were visualized using ethidium bromide staining. Glyceraldehyde-3-phosphate dehydrogenase (GAPDH) was used as the internal control.

Statistical analysis

The statistical analysis utilized two-way ANOVA, complemented by the Tukey post hoc test, to assess significance across different data sets. Two-way ANOVA was chosen to evaluate the interaction effects between multiple independent variables on the dependent variables, ensuring a comprehensive analysis of the experimental outcomes. The Tukey post hoc test was employed to perform pairwise comparisons while controlling for Type I errors, making it a suitable method for identifying significant differences between groups. The significance levels were categorized as follows: not significant (ns) for p-values ≥ 0.05, * for $p < 0.05$, ** for $p < 0.01$, *** for $p < 0.001$, and **** for $p < 0.0001$. All statistical analyses were performed using GraphPad Prism version 9.5.0, and data were presented as mean ± standard deviation (SD) unless otherwise stated.

Results and discussions

Fabrication of scaffolds

Scaffolds were constructed by blending bioceramic and Alg/SF polymer matrices (Fig. 2A), followed by cross-linking with GA or BDDE (Fig. 2B). The blends were poured into molds and lyophilized to obtain biomimetic scaffolds for the BTE. Initially, scaffolds were formulated with 4–8 wt.% SF solution to assess their surface properties. Through trial and error, it was determined that the 6 wt.% SF solution enabled the scaffolds to gel quickly and retain an adequate β-sheet content for subsequent assessments [55]. Increasing the SF concentration affects molding process and the shape fidelity of the scaffold, which is likely due to the higher hydrophobicity of SF. Studies have shown that GA concentrations >0.5 wt.% in the scaffold are toxic to cells and reduce cell proliferation [56]. Therefore, we used either GA or BDDE as cross-linkers at the lowest possible concentration for scaffold preparation. To minimize potential cytotoxicity, the cross-linked scaffolds were thoroughly washed to remove any residual or unreacted cross-linkers trapped within the scaffolds. Importantly, the nHAp used in the scaffolds needed to be effectively dispersed without aggregation. Moreover, the synthesized nHAp exhibited a rod-like morphology with nanoscale dimensions, closely resembling the apatite crystals of natural bone (Fig. S1). In this study, nHAp was effectively dispersed at initial concentrations between 0.1 and 0.5 wt.%, while aggregation was observed at 0.6 wt.%. Biomimetic scaffolds were fabricated using original precursors consisting 6 wt.% SF, 0.5 wt.% HAp, and 1.5 wt.% Alg, cross-linked with either GA or BDDE, to obtain SNAG or SNAB scaffolds (Table 1). Scaffolds without crosslinking, termed SNAX, were also prepared and used as controls. In addition, SF/nHAp and Alg/SF scaffolds were prepared and used as controls. The cross-linked scaffolds were molded into various shapes, such as cylinders and rectangles, demonstrating their shape fidelity.

The three-dimensional porous structures of the prepared SF, SF/nHAp, Alg/nHAP, SNAX, SNAG and SNAB scaffolds were investigated using SEM (Fig. 3A). The aqueous-derived SF scaffolds exhibited pore diameters ranging from 10 to 200 μm. The presence of nHAp in the SF/nHAp scaffolds slightly increased the pore size to approximately 50–250 μm, likely owing to electrostatic and hydrogen bonding interactions. Both the purified SF and SF/nHAp scaffolds had similar porous structures, but the surface of the SF/nHAp scaffold was rougher owing to the addition of nHAp. In the polymer network, the dispersion of nHAp was homogeneous, with no significant aggregation, which is expected enhance cell adhesion and proliferation owing to the excellent biocompatibility of nHAp [57]. For the SNAX scaffold, the incorporation of polymers and bio-ceramics facilitated suitable adhesives, and bivalent cations such as Ca^{2+} from nHAp crosslinked the Alg polymers, resulting in pore sizes of approximately 10–200 μm. The addition of nHAp and Alg increased the surface roughness, with nHAp particle diameters ranging

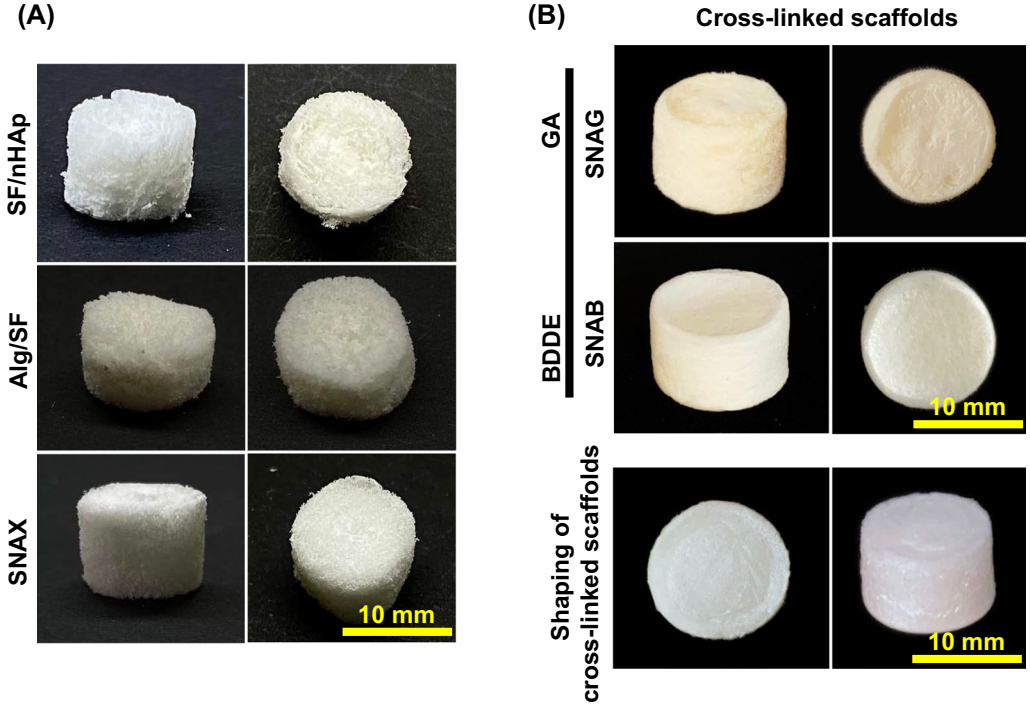

Fig. 2 Three-dimensional images of freeze-dried (**A**) SF/nHAp, Alg/SF, SF/nHAp/Alg (SNAX) scaffolds, (**B**) cross-linked SNAG and SNAB scaffolds and structure shaping of SNAB scaffolds.

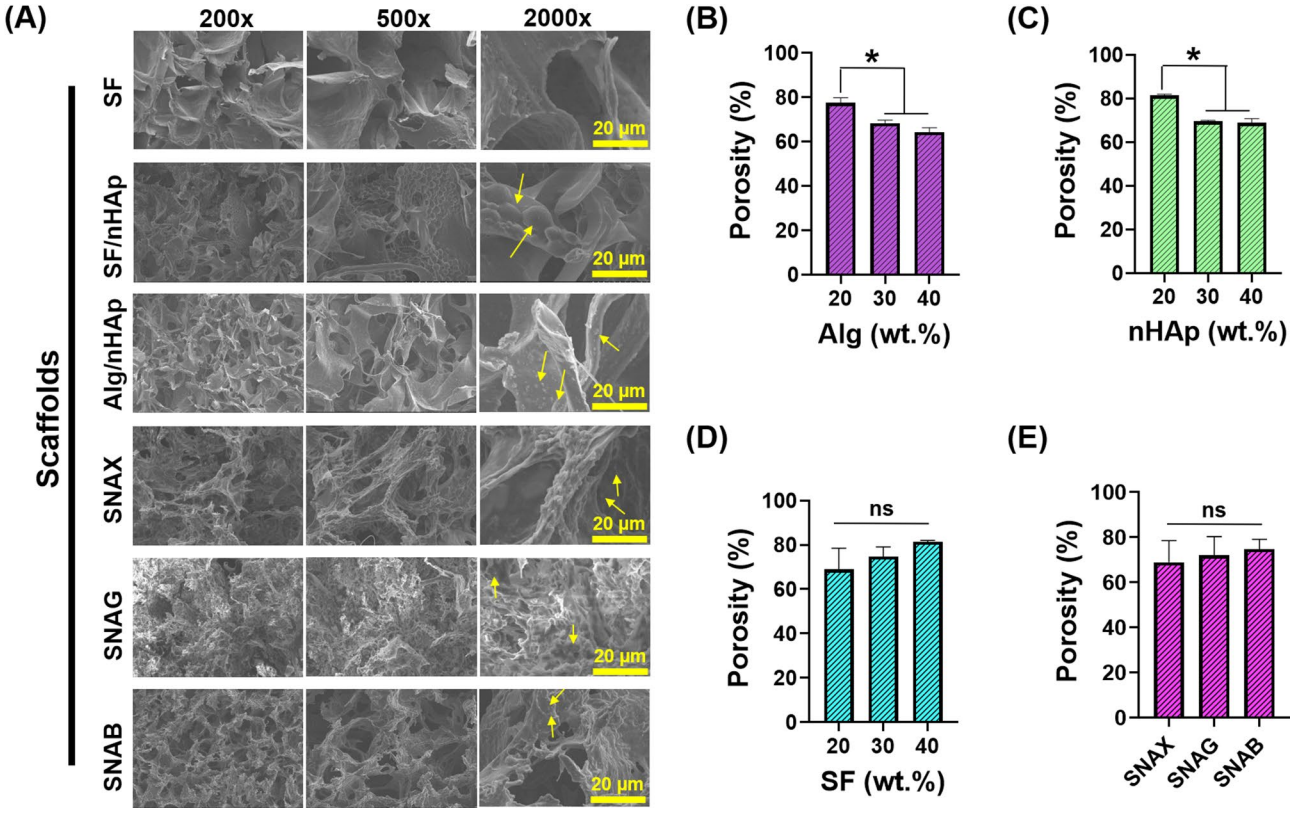

Fig. 3 (**A**) SEM images showing the cross-sectional morphology of the prepared scaffolds at different magnifications. Arrows indicate the distribution of nHAp within the hydrogel network. (**B**-**E**) Porosity of the scaffolds prepared with varying compositions of each component. *p < 0.05; 'ns' denotes no significant difference.

from 50 nm to 200 nm. These particles were uniformly distributed and maintained the scaffold structure owing to their reinforcement ability. In BTE, an ideal scaffold must be sufficiently porous to facilitate the exchange of nutrients, and enable cell adhesion [58]. Large pores with diameters of approximately 120–250 μm support cell migration and the provision of essentials [59], while smaller pores, around 10–150 μm in diameter, promote rapid and efficient cell proliferation and growth [60]. After cross-linking with GA, the SNAG scaffold's pore size was significantly reduced to less than 100 μm, mainly owing to the formation of multiple intra- and intermolecular cross-links between SF and Alg. The highly reactive nature of aldehydes with amine and alcohol groups facilitates the formation of Schiff bases and hemiacetal linkages in the scaffolds [61]. In contrast, the SNAB scaffolds, which were cross-linked with BDDE, were larger than the SNAG scaffolds. Unlike GA, BDDE exhibits lower activity toward the -NH_2 and -OH groups in polymers, which may account for the larger pore size.

In addition to the three-dimensional porous structure of the scaffolds, their porosities were examined after a controlled freeze-drying process (Fig. 3B-E). The scaffolds, fabricated using a freeze-drying process at −40 °C, exhibited high porosity (60–80%), which is essential for bone defect regeneration. For SF-based materials, an optimal porosity typically falls in range of 74% to 80%, supporting cell proliferation. The addition of 20% ratio of nHAp precursor increased porosity of the scaffold. However, from 30% ratio of nHAp, porosity significantly decreased. Although the inclusion of nHAp or similar particles aims to enhance porosity, the target of this study replied on achieving an optimal mixing ratio between nHAp and the polymers. An excessive amount of nHAp in the suspension increased the gel formation and viscosity, which hindered water vaporization and reduced the ice crystal formation during the freeze-drying process, thereby lowering the scaffold' porosity. Regardless of the other scaffold compositions, the SNAB scaffolds consistently exhibited the highest porosity (~80%).

In general, the three-dimensional porous architecture of scaffolds is critical for their performance in BTE. Recent studies continue to support the view that interconnected pores in the range of ~100–500 μm are favorable for facilitating cell infiltration, vascularization, and new bone formation [62, 63]. In our study, the SNAG scaffolds exhibited a reduced average pore size of <100 μm after cross-linking with glutaraldehyde (GA), primarily due to the formation of dense intra- and intermolecular cross-links. Although the pore size of SNAG

scaffolds was smaller than the commonly cited upper range, it still falls within ~50–150 μm, a range reported to support high cell adhesion, proliferation, and early extracellular matrix deposition [64]. Smaller pores can also increase the specific surface area available for cell attachment and enhance osteogenic differentiation at early stages [65]. In contrast, the SNAB scaffolds cross-linked with BDDE exhibited larger pores, closer to the upper end of the recommended range, which could facilitate vascular infiltration and support mature bone formation [66]. Overall, while the SNAB scaffolds offer advantages in preserving larger pore sizes, the SNAG scaffolds also exhibit biologically relevant porosity and functional performance, supporting their potential use in bone tissue engineering applications.

Characterization of scaffold

The cross-linked structure of the scaffolds was characterized by ^{1}H NMR spectroscopy. To assign the main characteristic peaks of free Alg and SF, they were dissolved in D_2O and their ^{1}H NMR spectra were measured. Fig. 4A and B show the ^{1}H NMR spectra of the Alg and SF, respectively. The anhydroglucose units of Alg appeared at 3.60 to 3.96 ppm, and the anomeric proton was assigned at 4.46 ppm. The ^{1}H NMR spectra of SF shows signals at 3.56 and 3.84 ppm, which are attributed to the serine and glycine residues. Additionally, major protein peaks corresponding to alanine, glycine, tyrosine, and valine in the primary SF structure were observed. Fig. 4C show the ^{1}H NMR spectra of GA-cross-linked SF without Alg. As expected, GA peaks appeared alongside SF peaks. Fig. 4D shows the ^{1}H NMR spectra of cross-linked SF with increasing feed molar ratios of BDDE. The characteristic signal at 1.51 ppm corresponds to the saturated hydrocarbon bonds formed between BDDE and the serine groups on the SF. As the initial concentration of BDDE was increased, the characteristic peak at 1.51 ppm gradually became more prominent. Fig. 4E shows the 1H NMR spectra of GA-crosslinked SF combined with Alg, displaying all characteristic peaks, including the Alg peaks corresponding to anomeric protons and anhydroglucose units. The FT-IR spectra in Fig. 5A and B show that both the starting materials and scaffolds reveal pronounced absorption bands at approximately 3300 cm^{-1}, indicating the presence of hydroxyl groups (O-H stretching). After crosslinking the SF/HAp/Alg scaffold with GA, a characteristic band appeared at 1660 cm^{-1}, which was assigned to the C=N stretching of imine residues formed by crosslinking lysine amino acids in SF with aldehyde in GA. After incubation with BDDE, the SNAB scaffolds exhibited lower absorption intensity at 3300 cm^{-1}, indicating consumption of hydroxyl and amine groups and the effective cross-linking in the scaffolds. Despite cross-linking, the three-dimensional structure of the SF protein remains unaltered. The presence of random coil and α-helix conformations was indicated by the band at 1640 cm^{-1}, while the β-sheet conformation, transformed from the random coil structure, was confirmed by the appearance of band around 1624 cm^{-1}, corresponding to the absorption peak of the peptide backbone of amide I (C=O stretching) [22]. The peak at 1528 cm^{-1} was attributed to amide II (N-H bending), and shifts in the absorption peaks at 1236 cm^{-1} indicated amide III (C-N stretching). Amides IV and V were observed at peaks around 694 cm^{-1} and 630 cm^{-1}, respectively. These characteristic absorbance peaks indicate the presence of hydrogen bonds. In addition to ionic interactions, the scaffold network is further enhanced by intra- and intermolecular hydrogen bonding, which arises from the amino acid sequences in SF and the interactions between functional groups of Alg and SF. The peaks at 1033 and 1088 cm^{-1} are assigned to the stretching vibration of the P-O bond in PO_4^{3-}, while the bands at 555 and 602 cm^{-1} correspond to the bending vibration of the O-P-O bond. Additionally, the O-H stretching vibrations observed at 3282 cm^{-1} [67]. The absorption bands at 1414 and 1444 cm^{-1} indicate the presence of CO_3^{2-} groups [68]. Furthermore, the diffraction patterns of nHAp were analyzed using XRD (Fig. 5C). The sharp and intense peak around 32 ° characterizes the (211) plane of hexagonal hydroxyapatite. Furthermore, diffraction peak attributed to hydroxyapatite is identified at 26 °, corresponds to (002) plane, strongly confirming the crystalline structure of nHAp. In contrast, the characteristic diffraction peaks were significantly diminished upon complexation with Alg, indicating the formation of the Alg/nHAp network.

Thermal and mechanical properties

The thermal stability of the SF, Alg, nHAp, SNAX, and SNAB scaffolds was determined using TGA (Fig. 5D). All materials exhibited distinct weight loss patterns in response to increasing temperature. The weight loss of SF and Alg began at 65–110 °C because of the evaporation of water molecules absorbed in the polymer chains. A more significant weight loss was observed between 260 °C and 280 °C for both SF and Alg, which was attributed to thermal decomposition. Interestingly, the residual weights of the SNAX and SNAB scaffolds increased, suggesting that the addition of nHAp enhanced the thermal stability of the scaffolds at high temperatures. As expected, nHAp exhibited a nearly flat curve after an initial weight loss at 120 °C and continued to plateau until 800 °C.

The mechanical properties of the scaffolds were evaluated using compression testing. Fig. 5E and F present the typical mechanical data. The cross-linked scaffolds exhibited significantly higher compressive strength than the non-cross-linked ones (i.e., SNAX), underscoring the importance of cross-linkers in providing the mechanical

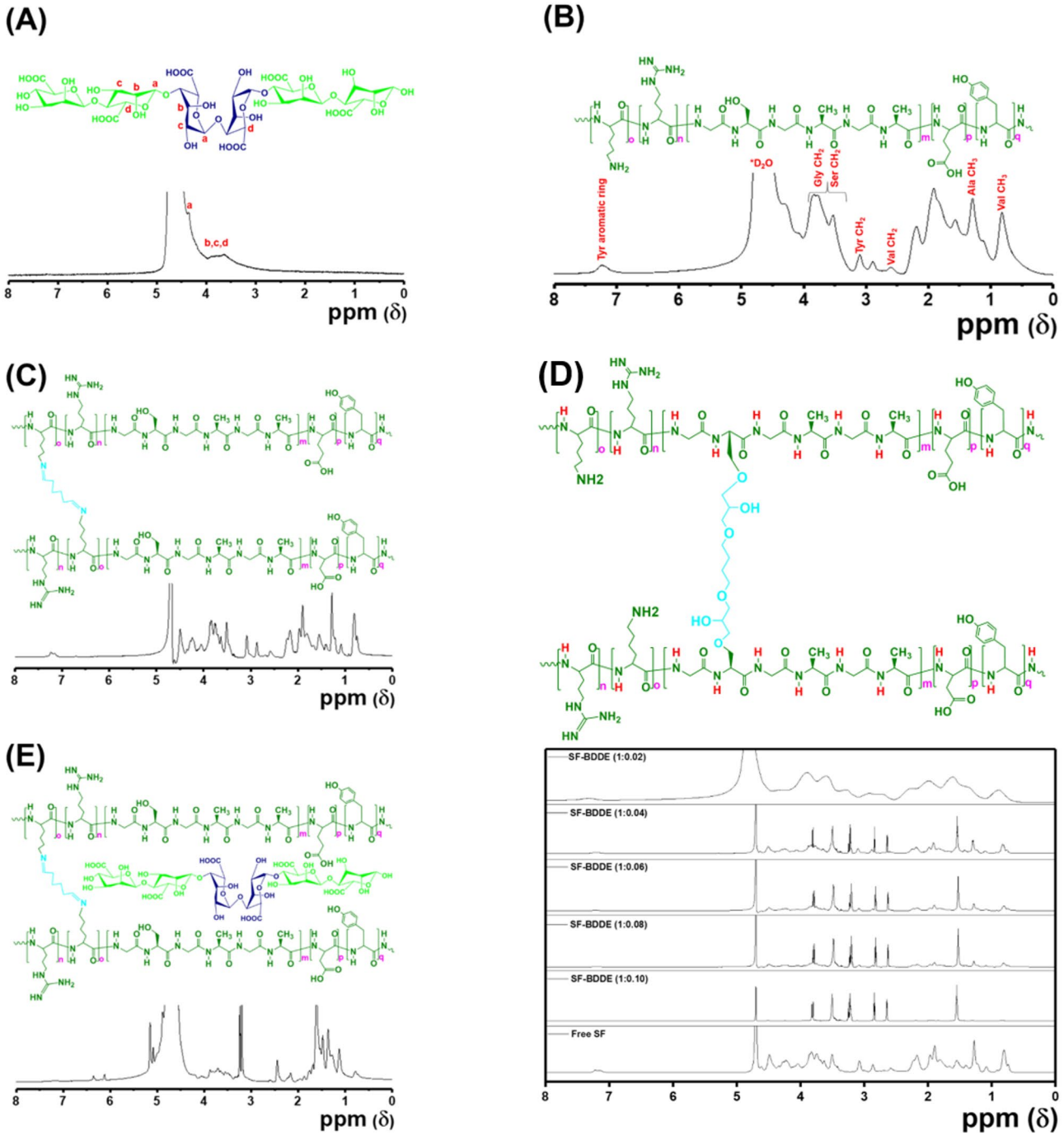

Fig. 4 ^{1}H NMR spectra of native (**A**) Alg and (**B**) SF polymers. (**C** and **E**) ^{1}H NMR spectra of GA cross-linked SF in the presence and absence of Alg. For this measurement, the SF was dissolved in D_2O and treated with GA and measure in situ analysis. (**D**) ^{1}H NMR spectra of BDDE cross-linked SF at various concentration of BDDE. Arrows indicate the gradual increase of BDDE cross-linker peaks. Asterisks (*) in the graph indicates residual solvent peaks.

stability and stiffness required for tissue engineering applications. Among the scaffolds, SNAB displayed the highest compressive strength, likely due to its homogeneous structure and enhanced flexibility. Although the SNAG scaffold also showed improved compressive strength, it did not surpass that of the BDDE-cross-linked scaffold. We hypothesize that GA, being a highly reactive and short-chain molecule, causes rapid local curing and increased brittleness. In contrast, BDDE promotes a milder reaction, facilitating the formation of a more uniform and flexible network.

Additionally, the static load-bearing capacity of the cylindrical SNAB scaffold was assessed using standard weights (1, 5, 20, 50, and 100 g). To this test, as shown in

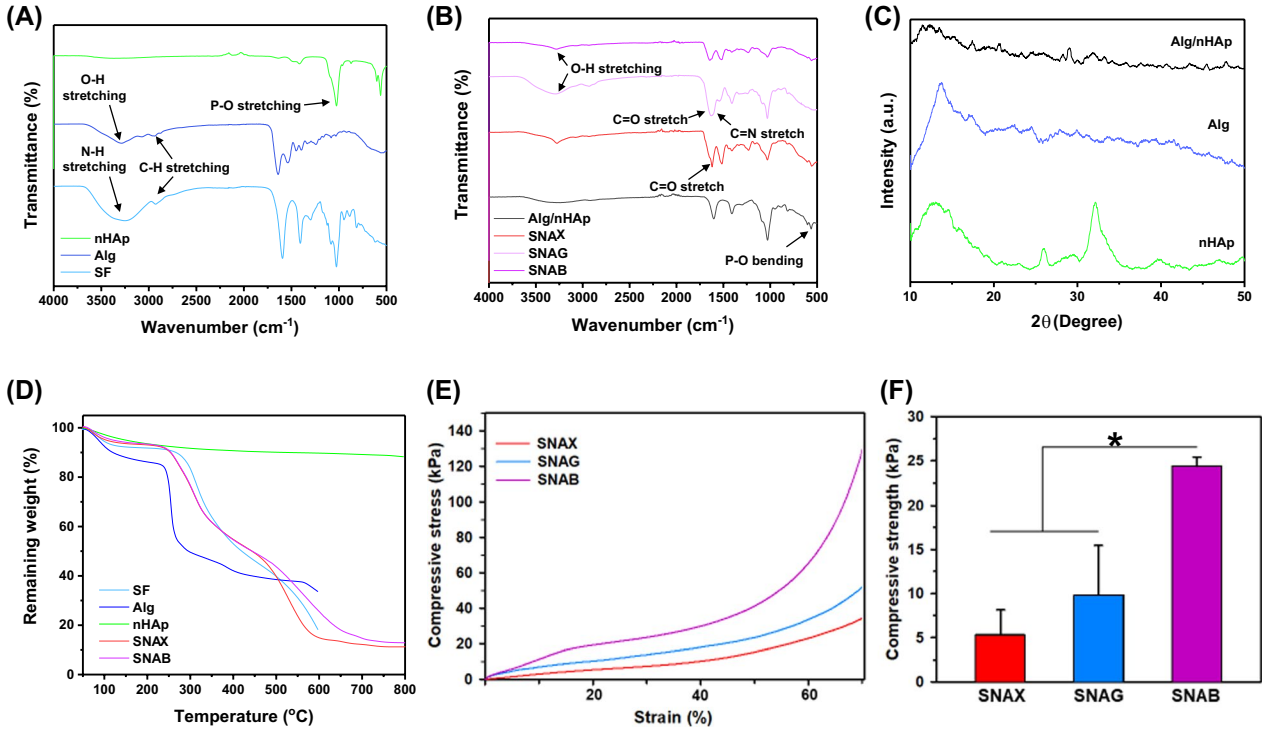

Fig. 5 FT-IR spectra of (**A**) nHAP, Alg, and SF and (**B**) Alg/nHAp, SNAX, SNAG and SNAB scaffolds. (**C**) XRD patterns of nHAp, Alg and Alg/nHAp scaffold. (**D**) TGA thermogram curves of native polymers and scaffolds. (E and F) Compressive stress–strain curves and comparison of compressive strength of SNAX, SNAG, and SNAB scaffolds. The SNAB scaffold exhibits the highest compressive stress at increasing strain, indicating superior mechanical stability compared to SNAX and SNAG. Error bars signify the standard deviation (SD) observed for three independent experiments. *p < 0.05.

Figure S2A and S2B, the scaffold withstood weights up to 50 g, with only a slight deformation, indicating its ability to bear a load of approximately 800 times its own weight. Compared to the regenerated SF hydrogel, which withstands a load of 735 times its own weight, our scaffold demonstrated significantly superior mechanical strength, which can be attributed to the chemical cross-linking and nHAp reinforcement within the cross-linked network structures [69]. It has been demonstrated that scaffolds with adequate mechanical strength can support the proliferation and differentiation of bone tissue cells, including osteoblasts, osteocytes, and osteoclasts [70].

Swelling ratio and stability of scaffolds

The high swelling capacity of biomaterials enhances scaffolds performance by promoting cell diffusion, effective immobilization, and improved biocompatibility. In SF, this swelling behavior is primarily attributed to its hydrophilic random coil domains [71]. As the percentage of SF increased, so did the swelling ratio. In addition, functional groups like –COOH and $–NH_2$ present in both SF and Alg can interact with the calcium ions and phosphate groups in nHAp, forming a network. As shown in Fig. 6A, the swelling degree decreased upon the incorporation of nHAp, likely due to the denser network formed between the polymers and nHAp restricted water uptake and diffusion. This swelling pattern is consistent with previously reported results. For instance, HAp incorporated into gelatin cryogels at increasing concentrations showed a decreased swelling ratio, and the introduction of HAp altered the swelling kinetics of the composite cryogels [72]. Similarly, polyacrylamide-carboxymethylcellulose hydrogel scaffolds incorporated with strontium- and selenium-doped bioceramics exhibited a similar swelling pattern. This can be explained by the strong ionic crosslinking between the negatively charged carboxylate groups (COO–) of carboxymethylcellulose and the divalent cations (e.g., Mg^{2+} and Sr^{2+}) [73].

Bone regeneration typically needs 6–8 weeks for the complete remodeling of bone defects. To simulate conditions in the human body, the scaffolds were immersed in PBS at room temperature for stability assessment. Scaffolds with different formulations were monitored for 30 days to assess their structural stabilization and ensure sufficient time for bone tissue regeneration. As shown in Figure 6B, the SF-based scaffolds exhibited good stability in PBS and maintained their shape. Notably, surface erosion in SNAB scaffold was significantly minimized compared to that in other scaffolds, indicating that chemical cross-linking enhanced the stability of the scaffolds.

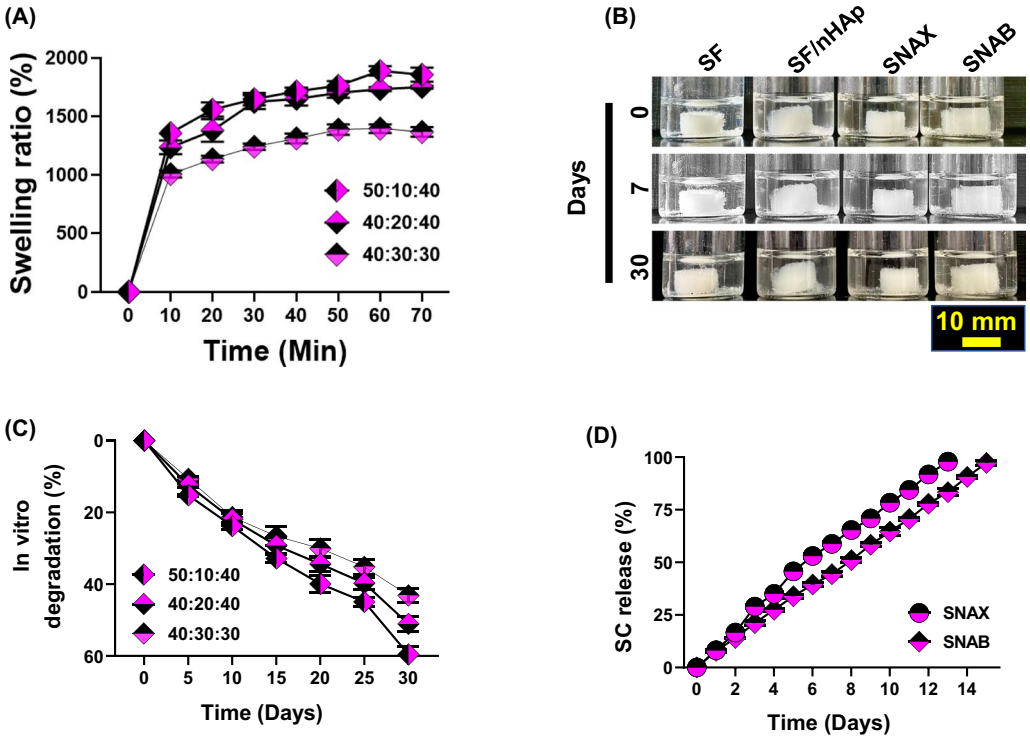

Fig. 6 (**A**) Swelling ratio (%) of scaffolds in PBS (pH 7.4 at 37 °C) as a function of time. (**B** and **C**) In vitro degradation images and in vitro degradation pattern of scaffolds in PBS (pH 7.4 at 37 °C) as a function of time. (**D**) In vitro release profiles of SC from scaffolds after incubation of SC-loaded scaffolds in PBS (pH 7.4 at 37 °C) as a function of time. Error bars signify the standard deviation (SD) observed for three independent experiments.

In vitro degradability

The controlled degradation patterns of the scaffolds were investigated by incubating them in PBS. Weight loss over time was then used to determine the degradation rate. This experiment demonstrated a controllable degradation rate for the scaffolds, reaching approximately 40–60% after 30 days (Fig. 6C). The ratio of the components within the scaffold influences this degradation, allowing for functionality within the human body. As detailed in the Materials section, higher contents of Alg and SF led to a faster degradation rate. Although typically non-degradable in the body, the ionically crosslinked Alg in this study could be broken down by reactions with common ions [74, 75]. Additionally, enzymes produced by osteoblasts during bone formation, such as alkaline phosphatase and bioactive compounds, further increase the degradability [76]. Conversely, scaffolds with higher nHAp content degraded more slowly due to the limited functional groups on the polymers from their interaction with nHAp, as well as the low solubility and structural reinforcement provided by nHAp. This trend aligns with previous studies, such as those on $CaSO_4$-based scaffolds, where the incorporation of nHAp significantly delayed degradation by reducing direct exposure to the immersion solution [77]. Similarly, in $CaCO_3$-based scaffolds, the degradation rate was inversely proportional to the nHAp content, with higher nHAp concentrations leading to slower weight loss over time [78]. These findings collectively highlight that controlling nHAp content is an effective strategy to modulate scaffold degradation, ensuring prolonged stability for sustained bone regeneration. This slow degradation provides long-term support and a gradual degradation window for new tissue growth.

In vitro SC release from the scaffolds

Incorporation of SC, even at low concentrations within the scaffolds, significantly impacted bone growth, particularly mineralization. The presence of nHAp in the scaffold structure facilitates drug delivery to bone tissues owing to its interaction with SC peptide chains. Additionally, SC effectively stimulates the osteogenic process in the bone. SC functions as a therapeutic drugs, supporting bone metabolism, inhibiting resorption, and critically modulating inflammatory and progenitor cells responses [79]. This ultimately leads to the formation of significant new tissue and promotes bone regeneration. In this study, the released SC was measured from 0 to 15 days at 1 day intervals. These frequent measurements were chosen to accurately capture the progression toward equilibrium. Fig. 6D shows the controlled release of SC from the scaffolds, avoiding an initial burst. This eliminates the risk of a massive early drug release, which can lead to excessive drug consumption and potentially

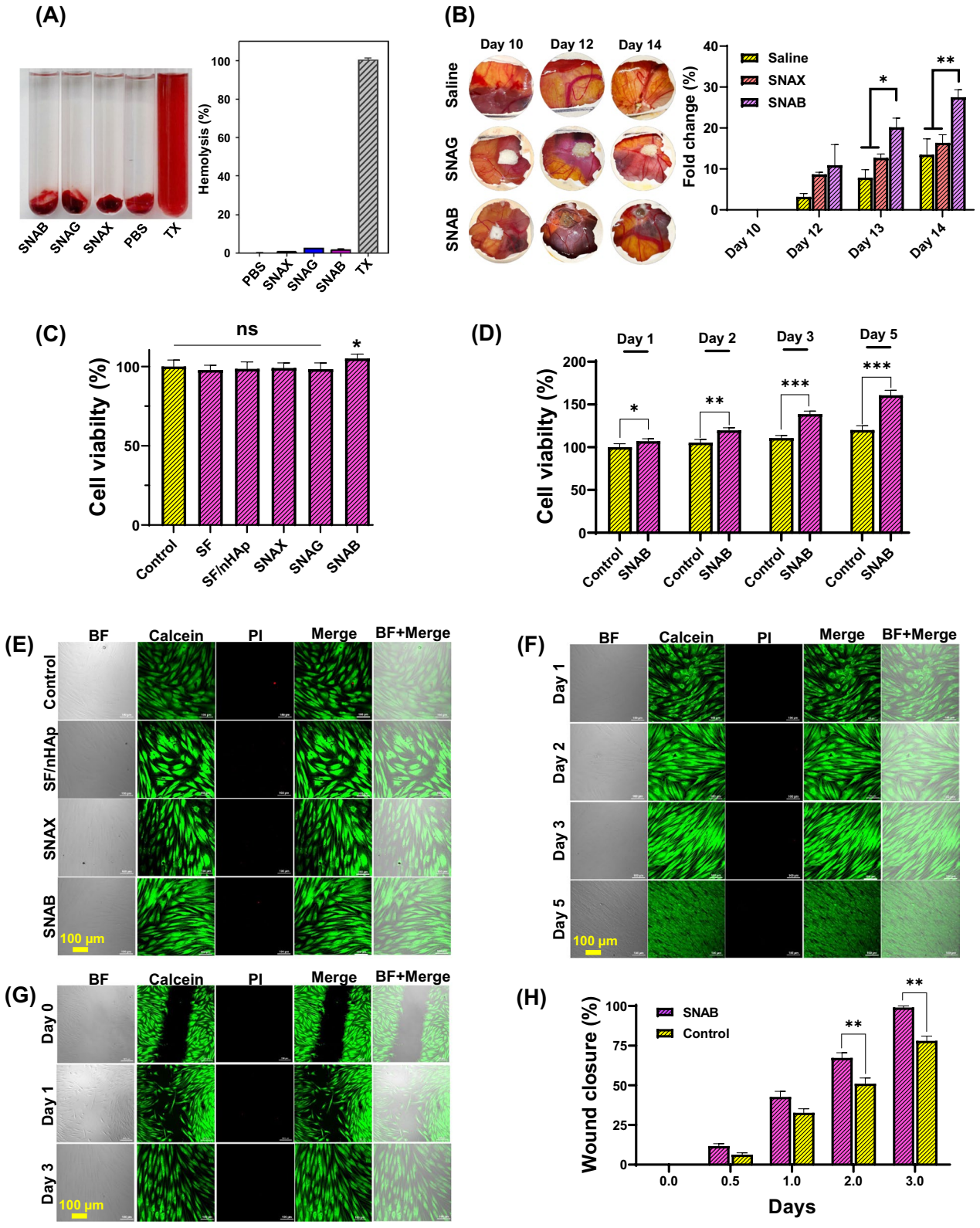

Fig. 7 (See legend on next page.)

(See figure on previous page.)

Fig. 7 In vitro safety of the scaffolds. (**A**) Images of test tubes containing RBCs after incubation with scaffolds for 3 h. The red solution indicates that the RBCs were destroyed and hemoglobin was released. TX represents positive control, and PBS represents negative control. Graph represents the hemolysis ratios of rabbit RBCs after the scaffolds were incubated with RBCs for 3 h at 37 °C with shaking 20 rpm. (**B**) *In ovo* CAM assay shows the biocompatibility and angiogenic response of scaffolds. Representative images show the appearance of blood vessels in chick embryo CAMs treated with scaffolds at different days. Quantitative analysis showed gradual increase in vascularized area as a function of time. (**C**) In vitro cytocompatibility HDF cells after treatment with scaffolds. (**D**) In vitro cell viability of scaffold cultured with HDF cells for 1, 2, 3, and 5 days. (**E**) Live and dead staining of HDF cells after incubating with scaffolds for 24 h. (**F**) Live and dead staining of HDF cells cultured with SNAB scaffolds at different days (1, 2, 3, and 5 days). (**G** and **H**) Wound healing assay of HDF cells after incubating with a SNAB scaffold, demonstrated that cell invasion into the cell-free region (outlined) is accelerated in the presence of SNAB scaffold. Summary bar graph illustrating percentage wound closure at indicated time points during the scratch wound assay. *p < 0.05, *p < 0.01, *p < 0.005, ***p < 0.001.

toxic systemic concentrations. Therefore, a controlled release profile minimizes the risk of exceeding the toxicity threshold of the drug.

Compared to previous studies, our scaffolds exhibit a more sustained release profile. For instance, size-switchable microspheres loaded with SC showed a burst release of over 40% within the first 24 h, whereas our system maintains a gradual release, ensuring prolonged therapeutic effects [80]. Similarly, SC-loaded nHAp and other nanocarriers underwent a rapid depletion phase, limiting long-term efficacy [81–83]. In contrast, our approach leverages the interaction between SC and nHAp, leading to a more stable and prolonged release, which is advantageous for bone tissue engineering. These findings indicate that our scaffold design offers improved drug retention and controlled delivery, aligning with the physiological demands of bone regeneration.

Hemocompatibility of the scaffolds

The hemocompatibility of scaffolds is a prerequisite for the materials used in BTE. First, the hemocompatibility of the scaffolds was tested by exposing them to red blood cells (RBCs). The hemolytic activity of the SNAX, SNAG, and SNAB scaffolds are shown in Fig. 7A. The RBCs exposed to the scaffold displayed a transparent color, similar to that of the PBS control group. As expected, the RBCs exposed to Triton X-100 turned bright red. Specifically, the hemolytic activity of the scaffolds were approximately lower 3%, confirming the good blood compatibility of the scaffolds [84] for BTE applications.

In ovo CAM assay

The CAM assay provides an accessible and cost-effective platform for evaluating the biocompatibility and angiogenic potential of biomaterials. As shown in Fig. 7B, a sterile scaffold was implanted into the eggshell on day 10 of incubation when the chick embryo was in critical stage of development. The scaffold came into direct contact with the CAM, and the embryo remained healthy without any signs of infection. By day 12, the formation of new blood vessels was evident, indicating normal embryonic development and early angiogenic response. The results recorded on days 12, 13 and 14 showed that angiogenesis continued and that other parts of the chick started to form. Notably, by day 14, the eggs implanted with SNAB scaffolds showed a significant enhancement in the vascularized area, when compared with the SNAG scaffold and Saline control. These findings confirm the scaffold's excellent biocompatibility and strong pro-angiogenic properties, which are essential attributes for applications in bone tissue engineering.

Cytocompatibility and cell proliferation of the scaffolds

One of the key factors hindering the application of scaffolds in BTE is their potential toxicity to cells as well as their negative impact on the bone regeneration process. HDFs were co-cultured with scaffolds to examine the cytocompatibility of the scaffolds. HDFs were selected as they play a crucial role in the initial stages of wound healing, extracellular matrix remodeling, and angiogenesis, which are also important for bone regeneration. As shown in Fig. 7C, the viability of HDF cells was not significantly affected, and in particular, the cells incubated with SNAB scaffolds showed slightly higher viability, indicating the non-toxic nature of the scaffolds.

To assess cell proliferation on the SNAB scaffolds, the proliferation of cells incubated with SNAB was continuously monitored over a period of 5 days (Fig. 7D). Remarkably, the viability of these cells remained high throughout the experiment and they were able to spread and proliferate over time, indicating that the scaffolds did not have a detrimental effect on the long-term viability of HDF. This pattern of cell proliferation was confirmed using a live/dead imaging assay (Fig. 7E and F), and the results were consistent with those obtained from the quantitative cell viability test. The imaging data corroborated that the various scaffolds proposed here were conducive to cell growth and viability [85]. These results demonstrate the feasibility of using scaffolds with excellent biocompatibility for tissue-engineering applications.

In vitro wound healing assay

Wound healing assay, also known as the in vitro scratch assay, is a common technique used in cell biology to study cell migration and wound repair processes. This method involves creating a "scratch" in a confluent monolayer of cells cultured on a surface, and then quantifying the ability of the cells to migrate and close the gap over time with

the application of biomaterials. In this study, the ability of a scaffold to accelerate the closure of simulated wounds in vitro was evaluated. If a scaffold formulation promotes faster wound closure in the assay, it suggests its potential efficacy in promoting tissue regeneration, which may translate to bone regeneration effects in vivo.

The scratch assay method was used to evaluate the wound closure effects of the biomimetic scaffolds in HDF cells (Fig. 7G and H). Wound closure started within 24 h for the biomimetic scaffolds. Notably, the extent of wound closure in the scaffold group was significantly higher than that in the untreated control group, which received only culture medium. Furthermore, complete wound closure was observed within 3 days in the scaffold group, whereas approximately 79% of the scratch wound was closed in the control group. This acceleration of the wound healing process indicates that the SNAB biomaterial is a promising scaffold for tissue regeneration applications.

In vitro hMSCs proliferation and osteogenic differentiation

The influence of various scaffolds on the proliferation of hMSCs was investigated by culturing the cells with the different scaffold types. The results from the live/dead assay after 72 h of culturing with the different scaffolds are presented in Fig. 8A. The cells displayed healthy growth, and no significant differences in proliferation were visible from the images. These findings suggest that the scaffolds developed in our study demonstrated good biocompatibility. Furthermore, the combination of Alg and SF in the scaffolds improved their ability to promote cell proliferation.

Notch signaling is known to play a vital role in the differentiation of hMSCs into osteoblasts. Previous reports have shown that SF protein promotes osteoblast differentiation by inhibiting Notch signaling, leading to an upregulation of markers like alkaline phosphatase (ALP), which further supports cell proliferation and differentiation [86]. ALP is a well-established early marker of osteogenic differentiation in mesenchymal stem cells and osteoblasts. During the initial stages of bone formation, ALP expression increases significantly, reflecting the cells' commitment toward an osteoblastic phenotype and their ability to promote mineralization by providing phosphate groups for hydroxyapatite deposition [87]. Therefore, ALP was selected for immunocytochemistry in this study as it allows us to assess the osteogenic potential of the cells cultured on the scaffolds at an early differentiation stage. As shown in Fig. 8B and Fig. S3, hMSCs cultured with SNAX and SNAB scaffolds exhibited a higher level of ALP expression compared to the control and SF/nHAP scaffold groups. Additionally, Alizarin red staining was employed to assess the formation of calcium-rich nodules. Fig. 8C shows a greater amount of Alizarin red staining in the SNAX and SNAB scaffold groups.

Inflammatory and osteogenic effects of biomimetic scaffolds in vivo

To assess the impact of biomimetic scaffolds on inflammation, we tracked the levels of IL-6 and IL-8 two weeks after implantation (Figure 9A). We performed RT-PCR analysis to determine whether the scaffolds reduced inflammation. As shown in Fig. 9B, proinflammatory cytokines such as IL-6 and IL-8 were significantly reduced in the scaffold group compared to the control group without treatment. These findings suggest that the biomimetic scaffold implantation suppresses the expression of proinflammatory cytokines.

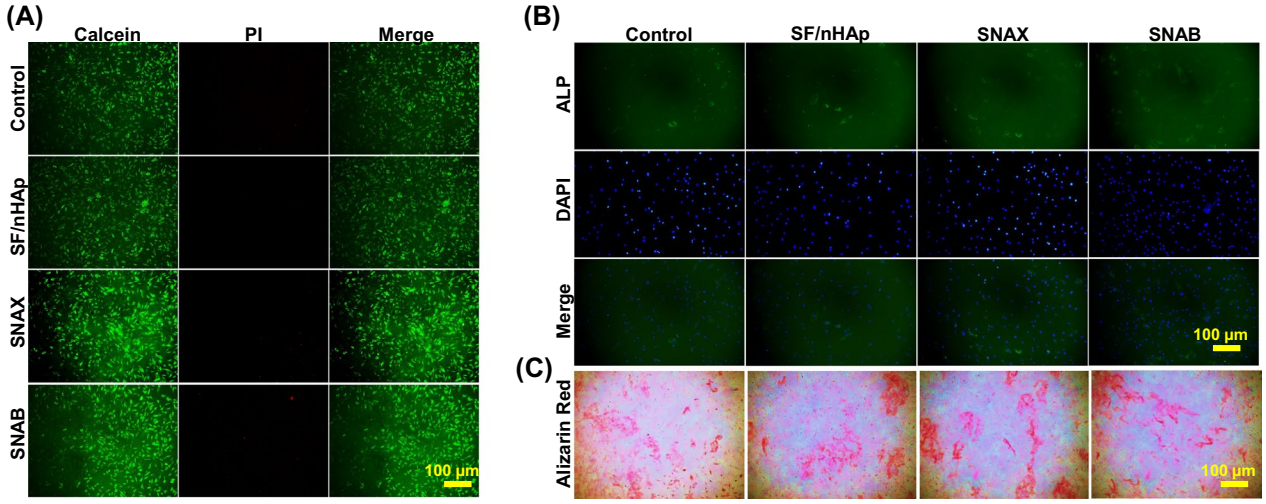

Fig. 8 (**A**) Fluorescence images showing live (calcein-AM, green) and dead (PI, red) staining of hMSCs grown on scaffolds. (**B**) ALP staining of hMSCs after 5 days of osteogenic differentiation on scaffolds. (**C**) Alizarin Red S staining showing calcium deposition in hMSCs cultured on scaffolds.

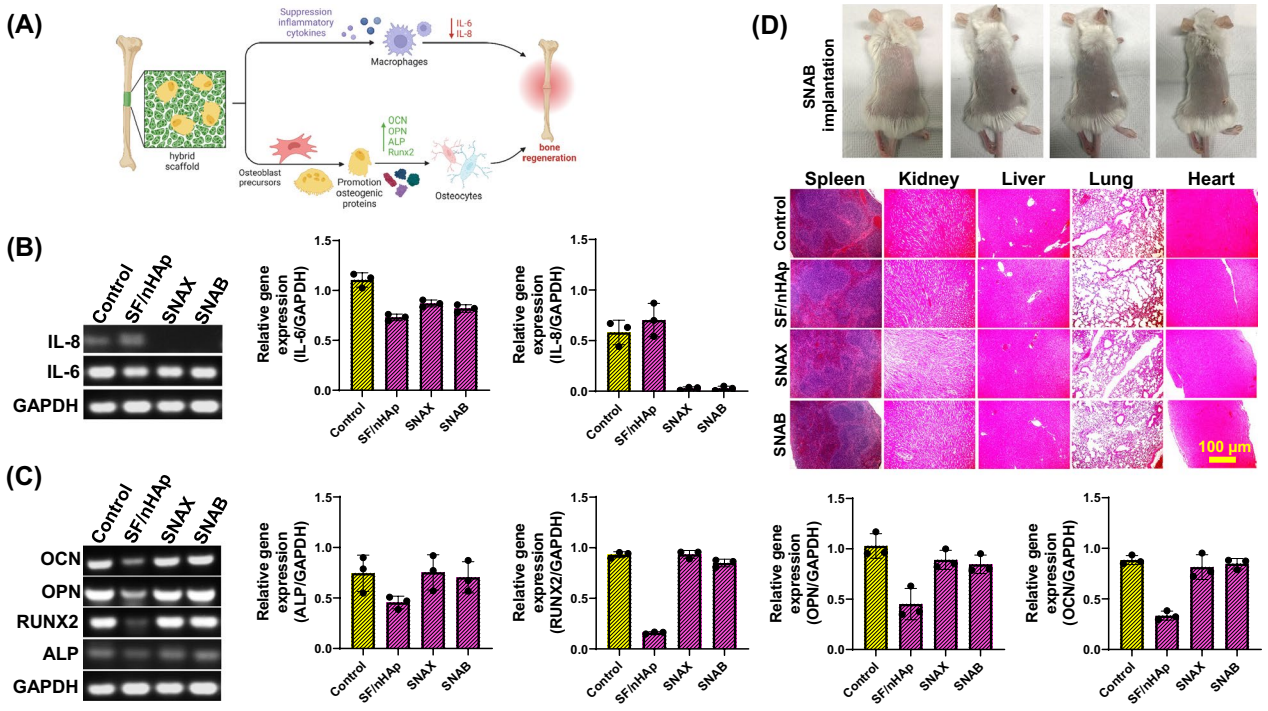

Fig. 9 (**A**) Schematic illustration of scaffold implantation and bone regeneration mechanism by suppressing the inflammatory cytokines and promoting osteogenic proteins. (**B** and **C**) RT-PCR analysis of mRNA extracted from mice after implanted with different scaffold formulations. The relative gene expression levels were analyzed using ImageJ. (**D**) In vivo implantation of SNAB into the mice. H&E staining images of major organs recorded two-weeks after implanted with different scaffold formulations.

Next, we investigated the influence of the scaffolds on osteoblast differentiation using RT-PCR to assess the gene expression of OCN, OPN, RUNX2, and ALP. RUNX2 plays a critical role in activating osteoblast differentiation, whereas OCN, OPN, and ALP are well-established osteogenesis markers. Notably, OCN is a late differentiation marker, explaining its higher expression than ALP, which peaks early and then declines. As shown in Fig. 9C, the SNAB scaffolds displayed a significant upregulation of OCN, OPN, and ALP compared to the SNAX scaffolds. These results indicated that biomimetic scaffolds can regulate the gene expression of osteoblasts, potentially promoting bone formation.

The gene expression analysis demonstrated that the SNAB and SNAX scaffolds significantly enhanced the expression of osteogenic markers RUNX2, ALP, OCN, and OCP compared to SF/nHAp. This superior functionality can be attributed to the biomimetic design of the scaffolds, which integrate nHAp with natural biopolymers such as SF and Alg, effectively mimicking the composition and architecture of the native bone extracellular matrix. Such a composite structure improves cell adhesion, proliferation, and differentiation by providing biochemical and mechanical cues absent in nHAp alone. Notably, the SNAB scaffold, crosslinked with BDDE, exhibited the highest osteogenic gene expression, likely due to its enhanced mechanical stability, interconnected porosity, and structural integrity, which create an optimal microenvironment for osteogenic differentiation. The crosslinked SNAB scaffold appears to support more sustained and consistent signaling to the cells, promoting their commitment to the osteogenic lineage. In contrast, although the SNAX scaffold (non-crosslinked) also performed better than SF/nHAp, the absence of crosslinking may result in suboptimal structural properties compared to SNAB, which could explain its relatively lower osteogenic potential.

In vivo safety of the biomimetic scaffolds

A major concern for the use of biomaterials in patients is their potential toxicity within the body. To assess the biocompatibility of our scaffolds, we implanted various scaffolds in mice after they reached a fully swollen state. Two weeks later, we examined the animals' major organs (heart, liver, spleen, lungs, and kidneys) for signs of damage using hematoxylin and eosin (H&E) staining. As shown in Fig. 9D, the organs from mice implanted with our scaffolds appeared similar to those of the control group, with no significant changes observed. This suggests good biocompatibility of the scaffolds in living organisms. The excellent biocompatibility of the SNAB scaffolds highlights their potential for tissue engineering applications.

While the results of this study are promising, several limitations need to be considered. First, the use of non-osteoblast cell lines in our in vitro experiments may not fully replicate the behavior of primary osteoblasts or the complexities of bone tissue. Future research should include osteoblast-like cell lines or primary cells to better mimic the in vivo bone regeneration process. Additionally, while the scaffolds demonstrated controlled release of SC and promising osteogenic potential in vitro, the absence of in vivo studies, particularly in bone defect repair models, limits the translation of these findings. In vivo testing is critical to evaluate the scaffolds' biocompatibility, degradation behavior, and long-term efficacy in promoting bone regeneration. Furthermore, the performance of the scaffolds may vary under physiological conditions, influenced by factors such as immune response, mechanical stress, and nutrient availability. Although the scaffolds demonstrated promising osteogenic potential in vitro and in a non-critical defect model, quantitative bone regeneration parameters such as bone volume/tissue volume and bone-specific marker expression at defect sites were not assessed in this study. These analyses will be prioritized in future critical-sized defect models to provide comprehensive validation of bone regeneration. These factors should be carefully considered in future studies to ensure the scaffolds' robustness and functionality in more complex environments.

We observed that the implanted scaffolds did not induce discernible histopathological changes in major organs after two weeks aligns with prior reports demonstrating the biocompatibility of hydrogel-based scaffolds for bone tissue engineering. For instance, Zhao et al. reported no significant inflammatory or fibrotic responses in liver, kidney, or spleen following implantation of electroactive injectable hydrogel in rats, supporting their systemic safety [88]. The favorable biocompatibility observed for the SNAB scaffolds may be attributed to the use of naturally derived components, such as SF and Alg, as well as the choice of crosslinking strategies that minimize cytotoxic residues. Notably, BDDE-crosslinked (SNAB) scaffolds exhibited particularly good biocompatibility, consistent with earlier findings that BDDE-crosslinked hydrogels elicit lower cytotoxic and inflammatory responses compared to glutaraldehyde-crosslinked counterparts [89].

Taken together, our results contribute to the growing body of evidence that appropriately designed and crosslinked biomimetic scaffolds can support tissue regeneration while maintaining systemic biocompatibility. Future work extending these findings into bone defect models and longer-term implantation studies will further elucidate the clinical potential of these scaffolds.

Conclusion

In this study, a biomimetic scaffold was successfully fabricated using biologically derived materials, including silk fibroin (SF) and alginate (SA), integrated with bone mineral-like nano-hydroxyapatite (nHAp). The resulting scaffold exhibited high porosity and an optimal pore size conducive to bone tissue regeneration. Additionally, the scaffolds showed favorable swelling and high durability in PBS, with a relatively strong load-bearing capacity. Notably, biomimetic scaffolds can effectively load synthetic SC peptides and release them in a sustained manner. In vitro studies demonstrated the high biocompatibility of the scaffolds, suggesting its safety for potential implantation into the human body. Moreover, the scaffold revealed excellent compatibility with red blood cells, as verified through hemolysis assays. Angiogenic properties were examined using the CAM assay, in which the scaffold was implanted in fertilized chicken eggs. The scaffold induced a pro-angiogenic response, leading to the development of microvasculature in adjacent tissues. Despite these promising results, the study has certain limitations, including the use of non-osteoblast cell lines and the absence of in vivo bone defect repair studies, which should be addressed in future research. Overall, SF/nHAp/Alg-based scaffolds prepared in this study are biocompatible, biodegradable, capable of controlling the release of synthetic peptides, and importantly, induce angiogenesis. These properties make them potentially useful in the biomedical field, particularly for bone regeneration.

Abbreviations

BTE	Bone tissue engineering
SF	Silk fibroin
Alg	Alginate
nHAp	Nanohydroxyapatite
SC	Salmon calcitonin
$CaCl_2$	Calcium chloride
$Ca(NO_3)_2.4H_2O$	Calcium nitrate tetrahydrate
BDDE	1,4-butanediol diglycidyl ether
SEM	Scanning electron microscopy
FTIR	Fourier transform infrared
XRD	X-ray diffraction
RBCs	Red blood cells
CAM	Chick embryo chorioallantoic membrane (CAM) assay
MTT	(3-(4, 5-dimethylthiazolyl-2)-2, 5-diphenyltetrazolium bromide)
RhB	Rhodamine B
DMEM	Dulbecco's modified eagle medium
PBS	Phosphate buffered saline

Supplementary Information

The online version contains supplementary material available at https://doi.org/10.1186/s12951-025-03816-x.

Additional file 1.

Acknowledgements

Not applicable.

Author contributions
Conceptualization, T.M.N.N., N.H.H.L., M.M., and T.T.; methodology, T.M.N.N., N.H.H.L., M.M., C.H.L., V.H.G.P.; validation, G.J., P.M., and S.V.; formal analysis, D.P., C.H.L., P.M., and E.S.J.; Resources, T.T.; S.V.; and E.S.J.; investigation, T.T.; writing—original draft preparation, T.T and M.M.; writing—review and editing, T.T., S.V., J.C.; supervision, T.T.; project administration, E.J., and T.T.; funding acquisition, E.J., Y.L., J.C., and T.T. All authors read and approved the final manuscript.

Funding
J. Conde acknowledges the national funds through FCT - Fundação Ciência e a Tecnologia, I.P., within the scope of UID/04923 and the FCT Grant LISBOA2030-FEDER-00862500-14998.
This work is supported by the National Research Foundation of Korea (NRF) grant funded by the Korea government (MSIT) (NRF-2023R1A2C1005904) and Zhejiang Provincial Natural Science Foundation (LY22E030012). This work was also supported by Ton Duc Thang University. E.-S.J. is incredibly grateful for the research grant from the Korean Ministry of Education, Science & Technology (2016R1D1A3B0201175615).

Data availability
The data presented in this study are available on request from the corresponding author.

Declarations

Ethics approval and consent to participate
All the animal experiments were approved by the Institutional Committees of Kyung Hee University (Approval number: KHU-22–216). The animal experiments were complied with the National Research Council's Guide for the Care and Use of Laboratory Animals.

Competing interest
J.C. is a co-founder and shareholder of TargTex S. A. -Targeted Therapeutics for Glioblastoma Multiforme. J.C. is a member of the Global Burden Disease (GBD) Consortium of the Institute for Health Metrics and Evaluation (IHME), University of Washington (US), and the Scientific Advisory Board of Vector Bioscience, Cambridge. The other authors declare no competing financial interests and have approved the final submission.

Author details
[1]Department of Chemistry, Faculty of Science and Technology, University of Lille, Lille, France
[2]Biomaterials and Nanotechnology Research Group, Faculty of Applied Sciences, Ton Duc Thang University, Ho Chi Minh City, Vietnam
[3]Graduate School of Biotechnology, College of Life Sciences, Kyung Hee University, Yongin si, Gyeonggi do 17104, Republic of Korea
[4]The Vijay Lab, Division of Engineering, New York University Abu Dhabi, Abu Dhabi, United Arab Emirates
[5]Department of Applied Chemistry, Kumoh National Institute of Technology, Daehak-ro 61, Gumi, Gyeongbuk 39177, Republic of Korea
[6]Queensland Micro- and Nanotechnology Centre, Griffith University, Nathan, QLD 4111, Australia
[7]College of Materials and Textile Engineering, Nanotechnology Research Institute, Jiaxing University, Zhejiang Province, Jiaxing 314001, PR China
[8]Comprehensive Health Research Centre (CHRC), NOVA Medical School|Faculdade de Ciências Médicas, NMS|FCM, Universidade NOVA de Lisboa, 1169-056 Lisbon, Portugal
[9]Queen's University Belfast, Belfast, United Kingdom
[10]Department of Marine Biotechnology, AMET University, Chennai-603112, Tami Nadu, India

Received: 25 March 2025 / Accepted: 25 October 2025
Published online: 01 December 2025

References

1. Guo J, Huang X, Dou L, Yan M, Shen T, Tang W, et al. Aging and aging-related diseases: from molecular mechanisms to interventions and treatments. Signal Transduct Target Ther. 2022;7:391.
2. Furman D, Campisi J, Verdin E, Carrera-Bastos P, Targ S, Franceschi C, et al. Chronic inflammation in the etiology of disease across the life span. Nat Med. 2019;25:1822–32.
3. Zhu G, Zhang T, Chen M, Yao K, Huang X, Zhang B, et al. Bone physiological microenvironment and healing mechanism: basis for future bone-tissue engineering scaffolds. Bioact Mater. 2021;6:4110–40.
4. Rupp M, Klute L, Baertl S, Walter N, Mannala G-K, Frank L, et al. The clinical use of bone graft substitutes in orthopedic surgery in Germany—a 10-years survey from 2008 to 2018 of 1,090,167 surgical interventions. J Biomed Mater Res B Appl Biomater. 2022;110:350–7.
5. Kim T, See CW, Li X, Zhu D. Orthopedic implants and devices for bone fractures and defects: past, present and perspective. Engineered Regeneration. 2020;1:6–18.
6. Migliorini F, Cuozzo F, Torsiello E, Spiezia F, Oliva F, Maffulli N. Autologous bone grafting in trauma and orthopaedic surgery: an evidence-based narrative review. J Clin Med. 2021. https://doi.org/10.3390/jcm10194347.
7. Wang W, Yeung KWK. Bone grafts and biomaterials substitutes for bone defect repair: a review. Bioact Mater. 2017;2(4):224–47.
8. Sohn H-S, Oh J-K. Review of bone graft and bone substitutes with an emphasis on fracture surgeries. Biomater Res. 2019;23:9.
9. Koons GL, Diba M, Mikos AG. Materials design for bone-tissue engineering. Nat Rev Mater. 2020;5(8):584–603.
10. Han F, Wang J, Ding L, Hu Y, Li W, Yuan Z, et al. Tissue engineering and regenerative medicine: achievements, future, and sustainability in Asia. Front Bioeng Biotechnol. 2020;8:83.
11. Lee SS, Du X, Kim I, Ferguson SJ. Scaffolds for bone-tissue engineering. Matter. 2022;5(9):2722–59.
12. Koushik TM, Miller CM, Antunes E. Bone tissue engineering scaffolds: function of multi-material hierarchically structured scaffolds. Adv Healthc Mater. 2023;12:2202766.
13. Turnbull G, Clarke J, Picard F, Riches P, Jia L, Han F, et al. 3D bioactive composite scaffolds for bone tissue engineering. Bioact Mater. 2018;3:278–314.
14. Yazdanpanah Z, Johnston JD, Cooper DML, Chen X. 3D bioprinted scaffolds for bone tissue engineering: state-of-the-art and emerging technologies. Front Bioeng Biotechnol. 2022;10:824156.
15. Zhao X, Li Q, Guo Z, Li Z. Constructing a cell microenvironment with biomaterial scaffolds for stem cell therapy. Stem Cell Res Ther. 2021;12:583.
16. Vepari C, Kaplan DL. Silk as a biomaterial. Prog Polym Sci. 2007;32:991–1007.
17. Asakura T, Okushita K, Williamson MP. Analysis of the structure of *Bombyx mori* silk fibroin by NMR. Macromolecules. 2015;48:2345–57.
18. Reizabal A, Costa CM, Pérez-Álvarez L, Vilas-Vilela JL, Lanceros-Méndez S. Silk fibroin as sustainable advanced material: material properties and characteristics, processing, and applications. Adv Funct Mater. 2023;33:2210764.
19. Koh L-D, Cheng Y, Teng C-P, Khin Y-W, Loh X-J, Tee S-Y, et al. Structures, mechanical properties and applications of silk fibroin materials. Prog Polym Sci. 2015;46:86–110.
20. Huang W, Ling S, Li C, Omenetto FG, Kaplan DL. Silkworm silk-based materials and devices generated using bio-nanotechnology. Chem Soc Rev. 2018;47:6486–504.
21. Patel M, Dubey DK, Singh SP. Phenomenological models of *Bombyx mori* silk fibroin and their mechanical behavior using molecular dynamics simulations. Mater Sci Eng C Mater Biol Appl. 2020;108:110414.
22. Phan VHG, Murugesan M, Nguyen PPT, Luu CH, Le N-HH, Nguyen HT, et al. Biomimetic injectable hydrogel based on silk fibroin/hyaluronic acid embedded with methylprednisolone for cartilage regeneration. Colloids Surf B Biointerfaces. 2022;219:112859.
23. Zastulka A, Clichici S, Tomoaia-Cotisel M, Mocanu A, Roman C, Olteanu CD, et al. Recent trends in hydroxyapatite supplementation for osteoregenerative purposes. Materials. 2023. https://doi.org/10.3390/ma16031303.
24. Jeong J, Kim JH, Shim JH, Hwang NS, Heo CY. Bioactive calcium phosphate materials and applications in bone regeneration. Biomater Res. 2019;23:4.
25. Zhou H, Lee J. Nanoscale hydroxyapatite particles for bone tissue engineering. Acta Biomater. 2011;7:2769–81.
26. Maeno S, Niki Y, Matsumoto H, Morioka H, Yatabe T, Funayama A, et al. The effect of calcium ion concentration on osteoblast viability, proliferation and differentiation in monolayer and 3D culture. Biomaterials. 2005;26:4847–55.
27. Lee MN, Hwang H-S, Oh S-H, Roshanzadeh A, Kim J-W, Song JH, et al. Elevated extracellular calcium ions promote proliferation and migration of mesenchymal stem cells via increasing osteopontin expression. Exp Mol Med. 2018;50:1–16.

28. Al-Musawi MH, Turki S, Al-Naymi HAS, Sameer Al-salman S, Boroujeni VV, Alizadeh M, et al. Localized delivery of healing stimulator medicines for enhanced wound treatment. J Drug Deliv Sci Technol. 2024;101:106212.
29. Al-Naymi HAS, Al-Musawi MH, Mirhaj M, Valizadeh H, Momeni A, Danesh Pajooh AM, et al. Exploring nanobioceramics in wound healing as effective and economical alternatives. Heliyon. 2024. https://doi.org/10.1016/j.heliyon.2024.e38497.
30. Kim SH, Thambi T, Giang Phan VH, Lee DS. Modularly engineered alginate bioconjugate hydrogel as biocompatible injectable scaffold for in situ biomineralization. Carbohydr Polym. 2020;233:115832.
31. Janarthanan G, Lee S, Noh I. 3D printing of bioinspired alginate-albumin based instant gel ink with electroconductivity and its expansion to direct four-axis printing of hollow porous tubular constructs without supporting materials. Adv Funct Mater. 2021;31:2104441.
32. Phan VHG, Duong H-S, Le Q-GT, Janarthanan G, Vijayavenkataraman S, Nguyen H-NH, et al. Nanoengineered injectable hydrogels derived from layered double hydroxides and alginate for sustained release of protein therapeutics in tissue engineering applications. J Nanobiotechnol. 2023;21:405.
33. Phan VHG, Mathiyalagan R, Nguyen M-T, Tran T-T, Murugesan M, Ho T-N, et al. Ionically cross-linked alginate-chitosan core-shell hydrogel beads for oral delivery of insulin. Int J Biol Macromol. 2022;222:262–71.
34. Lee KY, Mooney DJ. Alginate: properties and biomedical applications. Prog Polym Sci. 2012;37:106–26.
35. Mao G, Tian S, Shi Y, Yang J, Li H, Tang H, et al. Preparation and evaluation of a novel alginate-arginine-zinc ion hydrogel film for skin wound healing. Carbohydr Polym. 2023;311:120757.
36. Jo Y-Y, Kim S-G, Kwon K-J, Kweon H, Chae W-S, Yang W-G, et al. Silk fibroin-alginate-hydroxyapatite composite particles in bone tissue engineering applications in vivo. Int J Mol Sci. 2017;18:858.
37. Meng Z-Y, Wang L, Shen L-Y, Li Z-H, Zhao Z, Wang X-Y. Supercritical carbon dioxide assisted fabrication of biomimetic sodium alginate/silk fibroin nanofibrous scaffolds. J Appl Polym Sci. 2021;138:51421.
38. Spessot E, Passuello S, Shah LV, Maniglio D, Motta A. Nanocomposite methacrylated silk fibroin-based scaffolds for bone tissue engineering. Biomimetics. 2024;9:218.
39. Ghorbani M, Vasheghani-Farahani E, Azarpira N, Hashemi-Najafabadi S, Ghasemi A. Dual-crosslinked in-situ forming alginate/silk fibroin hydrogel with potential for bone tissue engineering. Biomaterials Advances. 2023;153:213565.
40. Shao Y-F, Wang H, Zhu Y, Peng Y, Bai F, Zhang J, et al. Hydroxyapatite/silk fibroin composite scaffold with a porous structure and mechanical strength similar to cancellous bone by electric field-induced gel technology. ACS Appl Mater Interfaces. 2024;16:60977–91.
41. Xie J, Guo J, Kanwal Z, Wu M, Lv X, Ibrahim NA, et al. Calcitonin and bone physiology. In vitro, in vivo, and clinical investigations. Int J Endocrinol. 2020;2020:3236828.
42. Keller J, Catala-Lehnen P, Huebner AK, Jeschke A, Heckt T, Lueth A, et al. Calcitonin controls bone formation by inhibiting the release of sphingosine 1-phosphate from osteoclasts. Nat Commun. 2014;5(1):5215.
43. Lymperi S, Ersek A, Ferraro F, Dazzi F, Horwood NJ. Inhibition of osteoclast function reduces hematopoietic stem cell numbers in vivo. Blood. 2011;117:1540–9.
44. Baranowsky A, Jahn D, Jiang S, Yorgan T, Ludewig P, Appelt J, et al. Procalcitonin is expressed in osteoblasts and limits bone resorption through inhibition of macrophage migration during intermittent PTH treatment. Bone Res. 2022;10:9.
45. Yelten-Yilmaz A, Yilmaz S. Wet chemical precipitation synthesis of hydroxyapatite (HA) powders. Ceram Int. 2018;44:9703–10.
46. Tomić SL, Nikodinović-Runić J, Vukomanović M, Babić MM, Vuković JS. Novel hydrogel scaffolds based on alginate, gelatin, 2-hydroxyethyl methacrylate, and hydroxyapatite. Polymers. 2021;13:932.
47. Tavakoli M, Emadi R, Salehi H, Labbaf S, Varshosaz J. Incorporation of graphene oxide as a coupling agent in a 3D printed polylactic acid/hardystonite nanocomposite scaffold for bone tissue regeneration applications. Int J Biol Macromol. 2023;253:126510.
48. Al-Sudani BT, Salehi S, Kamil MM, Al-Musawi MH, Valizadeh H, Mirhaj M, et al. Highly porous 3D printed scaffold incorporated with graphene oxide-merwinite and coated with IGF1 loaded nanofibers for calvarial defect repair. J Polym Environ. 2024;32:5330–43.
49. Hanif S, Rehmat S, Hassan M, Majeed F, Islam A, Khan RU. Stimuli-responsive crosslinked chitosan/polyethylene glycol/3-glycidyloxypropyltrimethoxy silane-based hydrogels for biomedical applications. BME Horizon. 2024;2(1):102–102.
50. Pan T, Song W, Cao X, Wang Y. 3D bioplotting of gelatin/alginate scaffolds for tissue engineering: influence of crosslinking degree and pore architecture on physicochemical properties. J Mater Sci Technol. 2016;32:889–900.
51. Tran T-HH, Luu CH, Nguyen K-TT, Hoang M-AL, Pham Q-K, Phan CM, et al. Mineralized Biopolymers-Based Scaffold Encapsulating with Dual Drugs for Alveolar Ridge Preservation. Macromol Biosci. 2025;25:2400351.
52. Ngo P-KT, Nguyen DN, Nguyen H-P, Tran T-HH, Nguyen Q-ND, Luu CH, et al. Silk fibroin/chitosan/montmorillonite sponge dressing: enhancing hemostasis, antimicrobial activity, and angiogenesis for advanced wound healing applications. Int J Biol Macromol. 2024;279:135329.
53. Kazemi N, Javad Mahalati M, Kaviani Y, Al-Musawi MH, Varshosaz J, Soleymani Eil Bakhtiari S, et al. Core-shell nanofibers containing L-arginine stimulates angiogenesis and full thickness dermal wound repair. Int J Pharm. 2024;653:123931.
54. Talib Al-Sudani B, Al-Musawi MH, Kamil MM, Turki SH, Nasiri- Harchegani S, Najafinezhad A, et al. Vasculo-osteogenic keratin-based nanofibers containing merwinite nanoparticles and sildenafil for bone tissue regeneration. Int J Pharm. 2024;667:124875.
55. Kambe Y, Mizoguchi Y, Kuwahara K, Nakaoki T, Hirano Y, Yamaoka T. Beta-sheet content significantly correlates with the biodegradation time of silk fibroin hydrogels showing a wide range of compressive modulus. Polym Degrad Stabil. 2020;179:109240.
56. Zhang Y, Wang Q-S, Yan K, Qi Y, Wang G-F, Cui Y-L. Preparation, characterization, and evaluation of genipin crosslinked chitosan/gelatin three-dimensional scaffolds for liver tissue engineering applications. J Biomed Mater Res A. 2016;104:1863–70.
57. Wijerathne HMCS, Yan D, Zeng B, Xie Y, Hu H, Wickramaratne MN, et al. Effect of nano-hydroxyapatite on protein adsorption and cell adhesion of poly(lactic acid)/nano-hydroxyapatite composite microspheres. SN Appl Sci. 2020;2:722.
58. Ai C, Liu L, Goh JC-H. Pore size modulates in vitro osteogenesis of bone marrow mesenchymal stem cells in fibronectin/gelatin coated silk fibroin scaffolds. Mater Sci Eng: C. 2021;124:112088.
59. Swanson WB, Omi M, Zhang Z, Nam HK, Jung Y, Wang G, et al. Macropore design of tissue engineering scaffolds regulates mesenchymal stem cell differentiation fate. Biomaterials. 2021;272:120769.
60. Zhang Q, Lu H, Kawazoe N, Chen G. Pore size effect of collagen scaffolds on cartilage regeneration. Acta Biomater. 2014;10:2005–13.
61. Zhai Z, Edgar KJ. Polysaccharide aldehydes and ketones: synthesis and reactivity. Biomacromolecules. 2024;25:2261–76.
62. Huang D, Li Z, Li G, Zhou F, Wang G, Ren X, et al. Biomimetic structural design in 3D-printed scaffolds for bone tissue engineering. Mater Today Bio. 2025;32:101664.
63. Govindan R, Gu FL, Karthi S, Girija EK. Effect of phosphate glass reinforcement on the mechanical and biological properties of freeze-dried gelatin composite scaffolds for bone tissue engineering applications. Mater Today Commun. 2020;22:100765.
64. Pinto RV, Gomes PS, Fernandes MH, Costa MEV, Almeida MM. Glutaraldehyde-crosslinking chitosan scaffolds reinforced with calcium phosphate spray-dried granules for bone tissue applications. Mater Sci Eng C Mater Biol Appl. 2020;109:110557.
65. Yao Y-t, Yang Y, Ye Q, Cao S-s, Zhang X-p, Zhao K, et al. Effects of pore size and porosity on cytocompatibility and osteogenic differentiation of porous titanium. J Mater Sci Mater Med. 2021;32:72.
66. Mukasheva F, Adilova L, Dyussenbinov A, Yernaimanova B, Abilev M, Akilbekova D. Optimizing scaffold pore size for tissue engineering: insights across various tissue types. Front Bioeng Biotechnol. 2024;12:1444986.
67. Pyun DG, Yoon HS, Chung HY, Choi HJ, Thambi T, Kim BS, et al. Evaluation of AgHAP-containing polyurethane foam dressing for wound healing: synthesis, characterization, in vitro and in vivo studies. J Mater Chem B. 2015;3(39):7752–63.
68. Fleet ME. Infrared spectra of carbonate apatites: v2-region bands. Biomaterials. 2009;30:1473–81.
69. Gong D, Lin Q, Shao Z, Chen X, Yang Y. Preparing 3D-printable silk fibroin hydrogels with robustness by a two-step crosslinking method. RSC Adv. 2020;10:27225–34.
70. Li Y, Zhou M, Zheng W, Yang J, Jiang N. Scaffold-based tissue engineering strategies for soft–hard interface regeneration. Regen Biomater. 2022. https://doi.org/10.1093/rb/rbac091.

71. Tavsanli B, Okay O. Mechanically robust and stretchable silk/hyaluronic acid hydrogels. Carbohydr Polym. 2019;208:413–20.
72. Gu L, Zhang J, Li L, Du Z, Cai Q, Yang X. Hydroxyapatite nanowire composited gelatin cryogel with improved mechanical properties and cell migration for bone regeneration. Biomed Mater. 2019;14:045001.
73. Sarin N, Kurakula M, Singh KJ, Kumar A, Singh D, Arora S. Strontium and selenium doped bioceramics incorporated polyacrylamide-carboxymethylcellulose hydrogel scaffolds: mimicking key features of bone regeneration. J Asian Ceram Soc. 2021;9:531–48.
74. Li L, Zhao J, Sun Y, Yu F, Ma J. Ionically cross-linked sodium alginate/κ-carrageenan double-network gel beads with low-swelling, enhanced mechanical properties, and excellent adsorption performance. Chem Eng J. 2019;372:1091–103.
75. Malektaj H, Drozdov AD, deClaville Christiansen J. Mechanical properties of alginate hydrogels cross-linked with multivalent cations. Polymers. 2023;15:3012.
76. Cao Y, Wang B. Biodegradation of silk biomaterials. Int J Mol Sci. 2009;10:1514–24.
77. Zhou J, Yuan F, Peng S, Xie H, Wu P, Feng P, et al. Tunable degradation rate and favorable bioactivity of porous calcium sulfate scaffolds by introducing nano-hydroxyapatite. Appl Sci. 2016;6:411.
78. Zhong Q, Li W, Su X, Li G, Zhou Y, Kundu SC, et al. Degradation pattern of porous CaCO3 and hydroxyapatite microspheres in vitro and in vivo for potential application in bone tissue engineering. Colloids Surf B Biointerfaces. 2016;143:56–63.
79. Turner AG, Tjahyono F, Chiu WSM, Skinner J, Sawyer R, Moore AJ, et al. The role of the calcitonin receptor in protecting against induced hypercalcemia is mediated via its actions in osteoclasts to inhibit bone resorption. Bone. 2011;48:354–61.
80. Zhang X, Chen J, Cui Y, Cui Y, Yan G, Tang H, et al. A size-switchable microsphere loaded with salmon calcitonin as two-weekly dosing for osteoporosis therapy. Eur J Pharm Biopharm. 2024;205:114565.
81. Kotak DJ, Devarajan PV. Bone targeted delivery of salmon calcitonin hydroxyapatite nanoparticles for sublingual osteoporosis therapy (SLOT). Nanomed Nanotechnol Biol Med. 2020;24:102153.
82. Seyedahmadi M, Saeidifar M, Javadpour J, Rezaei HR. Preparation and characterization of 5-fluorouracil loaded cellulose and exosome nanocarriers: sustained release behavior and cytotoxicity studies. ChemSelect. 2023;8:e202300967.
83. Li Y, Xing L, Wang L, Liu X, Wu L, Ni M, et al. Milk-derived exosomes as a promising vehicle for oral delivery of hydrophilic biomacromolecule drugs. Asian J Pharm Sci. 2023;18:100797.
84. Molly F, Sean W, Mark S, Colleen M, Scott A, Don R: Standard practice for assessment of hemolytic properties of materials. American Society for Testing of Materials ASTM F756-00 2000.
85. Liu Q, Dai W, Gao Y, Dong L, Jia H, Li S, et al. The synergistic regulation of chondrogenesis by collagen-based hydrogels and cell co-culture. Acta Biomater. 2022;154:194–211.
86. Jung S-R, Song N-J, Yang DK, Cho Y-J, Kim B-J, Hong J-W, et al. Silk proteins stimulate osteoblast differentiation by suppressing the Notch signaling pathway in mesenchymal stem cells. Nutr Res. 2013;33:162–70.
87. Mollentze J, Durandt C, Pepper MS. An in vitro and in vivo comparison of osteogenic differentiation of human mesenchymal stromal/stem cells. Stem Cells Int. 2021;2021:9919361.
88. Zhao X, Wu H, Guo B, Dong R, Qiu Y, Ma PX. Antibacterial anti-oxidant electroactive injectable hydrogel as self-healing wound dressing with hemostasis and adhesiveness for cutaneous wound healing. Biomaterials. 2017;122:34–47.
89. Wang T, Li Y, Liu J, Fang Y, Guo W, Liu Y, et al. Intraarticularly injectable silk hydrogel microspheres with enhanced mechanical and structural stability to attenuate osteoarthritis. Biomaterials. 2022;286:121611.

Publisher's Note